

Silicon Photomultiplier Classification of the GCT Camera of CTA

Silicon Photomultiplier Klassifikation der GCT Kamera von CTA

Master-Thesis von Ben Gebhardt aus Heidelberg

Tag der Einreichung:

1. Gutachten: Dr. Richard White (MPIK)
2. Gutachten: Prof. Jim Hinton (MPIK)
3. Gutachten: Prof. Tetyana Galatyuk (TU DA)



TECHNISCHE
UNIVERSITÄT
DARMSTADT

Fachbereich Physik
Max Planck Institut für Kernphysik Heidelberg

8 Silicon Photomultiplier Classification of the GCT Camera of CTA
Silicon Photomultiplier Klassifikation der GCT Kamera von CTA

Vorgelegte Master-Thesis von Ben Gebhardt aus Heidelberg

1. Gutachten: Dr. Richard White (MPIK)
2. Gutachten: Prof. Jim Hinton (MPIK)
3. Gutachten: Prof. Tetyana Galatyuk (TU DA)

Tag der Einreichung:

¹⁰
¹¹ **Abstract**

¹² whats this about



Abstract

13
14
15 worum es geht



16 **Contents**

18	1 Cosmic Radiation	5
19	1.1 Air shower induced Cherenkov Radiation	7
20	1.2 Imaging Atmospheric Cherenkov Telescopes	8
21	2 Cherenkov Telescope Array	10
22	2.1 GCT	10
23	2.2 CHEC-S	11
24	2.3 SiPM requirements for CTA	12
25	3 Silicon Photomultipliers	14
26	3.1 Gain of a Silicon Photomultiplier	16
27	3.2 Thermally induced dark counts	17
28	3.3 Avalanche-induced secondary effects	18
29	3.4 OCT dependency on cellsize	19
30	3.5 Photon Detection Efficiency	20
31	4 Experimental Setup	22
32	5 Data Analysis	24
33	5.1 Tracefile Conversion	24
34	5.2 Pedestal Subtraction	25
35	5.3 Peak Detection	26
36	5.4 Gain Extraction	27
37	5.5 Data Challenges	29
38	6 Results	32
39	6.1 SiPM devices for CTA	32
40	6.2 Hamamatsu S12642-1616PA-50 50 μ m 3mm	34
41	6.3 Hamamatsu LCT5 50 μ m 6mm	39
42	6.4 Hamamatsu LCT5 75 μ m 7mm	43
43	6.5 Hamamatsu IVR 50 μ m 6mm	46
44	6.6 SensL FJ60035 6mm 35 μ m	49
45	7 Comparison	51
46	7.1 Dark Count Rate	51

47	7.2 Optical Cross Talk	52
48	7.3 Photon Detection Efficiency	54
49	7.4 Point of Operation Comparison	55
50	8 further analysis	56
51	8.1 multi incident probability and optical Cross Talk	56
52	8.2 Prompt and delayed cross talk ratio	56
53	9 Conclusion and Outlook	56
54	10 Glossary	57
55	11 Bibliography	58
56	12 Appendix	60

⁵⁷⁵⁸ 1 Cosmic Radiation

⁵⁹ Cosmic rays consist of a single particle with energies from 10^{10} to 10^{20} eV and describes extra-
⁶⁰ solar charged particles arriving on Earth and hitting the atmosphere fig(1). They were discovered
⁶¹ by V.F. Hess in 1912 during the famous balloon flight experiments. He aimed to measure the
⁶² conductivity of air, that until then, was believed to be an insulator resulting in some problems
⁶³ regarding the discharge of an electrically charged body, no matter how well it was isolated from
⁶⁴ the ground. Hess found the air's conductivity to increase with higher altitude, concluding the
⁶⁵ presence of a large amount of ionizing radiation above the atmosphere. The most energetic
⁶⁶ laboratory based accelerators operate in the 10^{12} eV energy range.
⁶⁷ Cosmic rays do not include those low energy particles originating from our sun. With a particle
⁶⁸ energy up to 1keV, those are referred to as solar wind, which means, by definition, cosmic rays
⁶⁹ arrive on Earth from outside our solar system. They consist of 87% protons, 12% α -particles
⁷⁰, 1% heavier nuclei and some electrons. High energy cosmic rays hitting Earth are very rare,
⁷¹ averaging to one per year in an area of one square kilometer. Except at those very high energies
⁷² ($>10^{18}$ eV) cosmic rays will not reach earth directly and can not be observed to pinpoint
⁷³ their source. Traveling through the interstellar medium, they get scattered by the interstellar
⁷⁴ magnetic fields, the cosmic microwave background and other hindrances and therefore have
⁷⁵ lost all directional information. However, directly observable cosmic rays, for example at the
⁷⁶ Pierre-Auger Observatory, provide an insight into cosmic particle accelerators.[3]

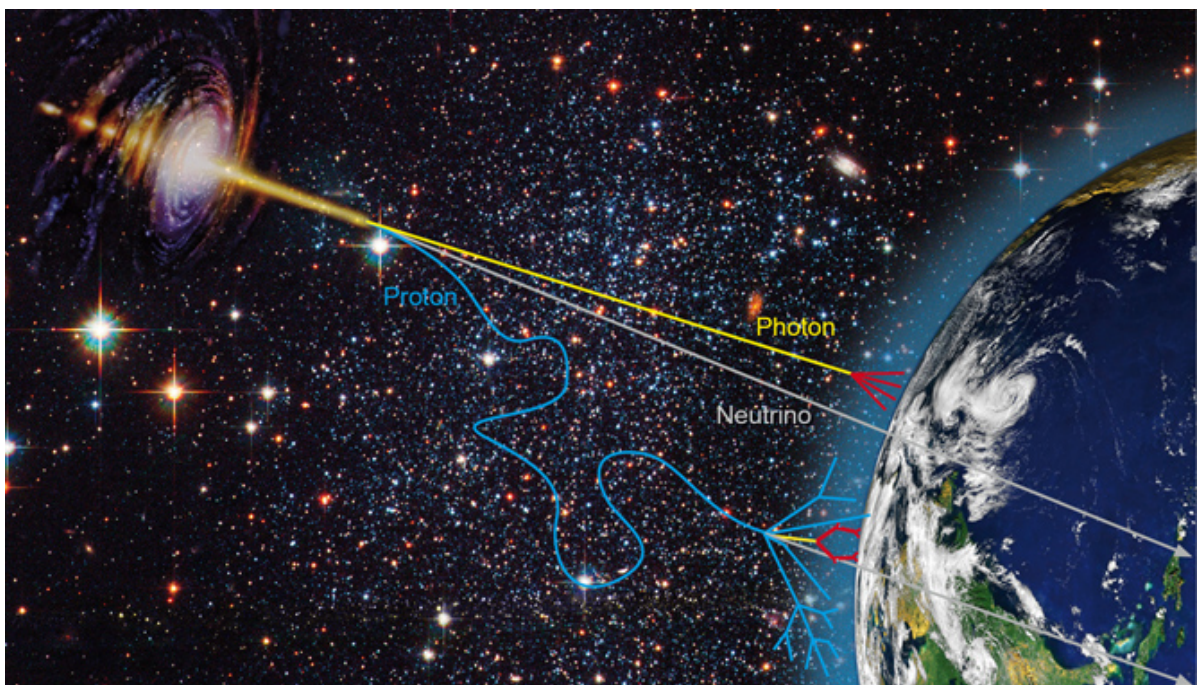


Figure 1: Gamma radiation photons (yellow) and scattered cosmic ray protons (blue) from an astrophysical source arriving on Earth. Neutrinos (grey) mostly do not interact. Picture from [17]

77 Cosmic rays of the higher energies are therefore observed via a detour: Gamma radiation.

78

79 Gamma radiation cannot be generated by
80 thermal emission of hot stellar objects, the
81 only event with a high enough temperature
82 to produce thermal radiation in the range of
83 GeV and TeV gamma radiation would be the
84 big bang, there is and has been nothing else
85 in the known universe. If thermal radiation
86 reflects the temperature of the emitting body,
87 what do gamma rays tell us?

88 Gamma radiation probe a non-thermal uni-
89 verse. In this one needs other mechanisms
90 to concentrate large amounts of energy into a
91 single quantum. The possible emission mechanisms are outlined below.

92 There are many diverse mechanisms of emitting gamma radiation. Gamma rays are generated
93 by high relativistic particles, in a first step for example: accelerated by the shockwave of a su-
94 pernova explosion. Those cosmic rays then collide with ambient gas, interact with photons or
95 magnetic fields, by inverse compton scattering, emitting high energy photons (down-top). Very-
96 high-energy (VHE) gamma radiation is defined as gamma radiation in the energy range of 10^{11}
97 to 10^{14} eV.



Figure 2: FermiLAT Picture from [18]

98 One such source of VHE gamma radiation and also the most famous, because the first to be
99 discovered, lies within the Crab Nebula. The Neutron Star located inside the Crab Nebula is a
100 Pulsar and the remnant of Supernova1054 and steadily emits gamma radiation energies up to
101 80 TeV. Another compound of the gamma radiation here is the so called Pulsar Wind Nebula. It
102 is composed of highly relativistic charged particles from the Pulsars giant rotating magnetic field
103 interacting with the expanding Supernova remnant via inverse compton scattering. Supernova
104 shockwaves themselves can also drive atomic nuclei to high energies which in turn emit observ-
105 able gamma-rays in a top-down fashion. Additionally, binary systems consisting of a black hole
106 or pulsar orbiting a massive star can emit a flow of high-energy particles with varying intensity,
107 based on the elliptical orbit, where particle acceleration conditions vary.

108 So just like thermal radiation reflects the temperature of the emitting object, the flux and en-
109 ergy spectrum of the gamma rays reflect the flux and spectrum of the high energy seed particles,
110 coming from the source. So they can be used to trace these cosmic rays and electrons in distant
111 regions of our own galaxy or even beyond.

112 One surprise was the discovery of so called "dark sources" , objects emitting VHE gamma-rays,
113 but have no counterpart in other wavelenghts, meaning those objects might only be observable
114 through gamma-rays. In extragalactical regions, gamma rays provide information on active

115 galaxies, where a constant stream of gas feeds a supermassive black hole at the center, releasing
116 enormous amounts of energy. From there, gamma rays are believed to be emitted, giving insight
117 into one of the most violent but to date poorly understood environments in our universe.

118 Even higher energy gamma rays could also be the product of decays of heavy particles, like
119 dark matter or cosmic strings. They therefore also provide a window to the discovery of dark
120 matter.

121

122 Gamma Radiation carries unique information about the most energetic phenomena in our
123 universe. The only problem is, our atmosphere is opaque for gamma radiation, gamma ray as-
124 tronomy in the lower energies is done by satellite based instruments like FermiLAT. The Large
125 Area Telescope, the principle scientific instrument on the Fermi Gamma-Ray Space Telescope
126 Spacecraft sensitive in the energy range between 20 MeV and 100 GeV, launched in June 2008.
127 fig (2) To reach the higher energy range through space based telescopes is very inconvenient,
128 since the required mass the telescope active area would need to detect the gamma rays increases
129 with gamma ray energy, and can therefore be very expensive to launch into space. Low energy
130 gamma rays can be efficiently captured by a volume appropriate for a spacecraft, for higher en-
131 ergy gamma rays using other interaction and detection media, like water or Earths atmosphere,
132 is more viable.

133 1.1 Air shower induced Cherenkov Radiation

135 The effect of gamma radiation on Earth is visible through gamma-ray induced particle cascades.
136 When a primary particle, i.e. a gamma photon or cosmic ray enters the atmosphere and collides
137 with a nucleus of the air, it gets scattered and creates secondary electrons, positrons and pho-
138 tons. Those secondary particles also interact with the atmosphere creating a cascade of particles
139 called a particle shower.

140 In this air shower, the initial and each subsequent particle traveling through our atmosphere
141 emits Cherenkov light. Cherenkov radiation is a phenomenon caused by charged particles
142 traveling faster than the local speed of light would allow in that medium. This light is emitted
143 in a narrow cone with an increasing angle as the particles travel downward. This Cherenkov
144 light shows as a very short ($\sim 5\text{ns}$) flash with a peak in the UV-spectrum at around 330nm. Thus,
145 we can image the particle cascade measured with the telescope and can reconstruct the direction
146 and energy through a stereoscopic image of the shower taken by multiple telescopes (see section
147 A), reconstructing the position of the source in the sky. It is also possible to reconstruct the
148 energy of the original photon from the amount of light produced, because energy is conserved,
149 so all energy of the original photon is now distributed between the particles of the shower.
150 To determine whether it is a hadronic shower, originating from cosmic rays, or a gamma shower,
151 originating from gamma ray photons, the shape of the shower and so called Hillas parameters

152 are used to determine the difference.

153 notes: IACTs HAWC FermiLAT

154 1.2 Imaging Atmospheric Cherenkov Telescopes

156 The technique, pioneered by the Wipple Collaboration,
157 behind the ground based experiments called Imaging
158 Atmospheric Cherenkov Telescope (IACTs) aims at
159 measuring the time, direction and energy of flashes
160 of Cherenkov light from extensive air showers caused
161 by VHE gamma radiation. Those ground based instru-
162 ments have a much larger effective detection area than
163 any satellite based instrument, which have a typical de-
164 tection size of 1m^2 . The range of the Cherenkov flash
165 being between 300-600nm, current generation Silicon
166 Photomultipliers (SiPMs) are a promising candidate to
167 replace the progenitor photon detector used in previ-
168 ous experiments like HESS, the Photomultiplier Tube
169 (PMT).

170 Current ground based IACT experiments are HESS,
171 MAGIC and Veritas. (see section B) HESS is the ...

172 Namibia consists of four telescopes the size of Xm op-
173 erating in the energy range of eV - eV. The recent HESS
174 upgrade added a fifth larger telescope in the center
175 of the array covering the xeV to XeV energy range.

176 MAGIC.... Veritas....

177 ——>All of those arrays consist of at most 5 telescopes spread over a wide area. So most
178 cascades are viewed by only 2 or 3 of the telescopes. Additionally, due to the low flux of VHE
179 gamma radiation, detectors for this energy range are spread over a large area, making space
180 based instruments, which detect the incident gamma ray, an inconvenient choice. Another
181 detection concept for VHE gamma radiation are ground based air shower particle detectors such
182 as the High-Altitude-Water-Cherenkov observatory (HAWC) [7]. It employs a similar detection
183 principle, recording shower particles reaching arrays of ground based particle detectors filled
184 with water as detection medium, in contrast to air in IACTs. Those have the advantage of a
185 larger duty cycle than IACTs, as they are able to operate during the day. Their limited sensitivity
186 even with high observation time however will not allow them to compete with the sensitivity
187 and resolution of IACTs such as in the CTA. The array will however be able to provide useful
188 complementary information.

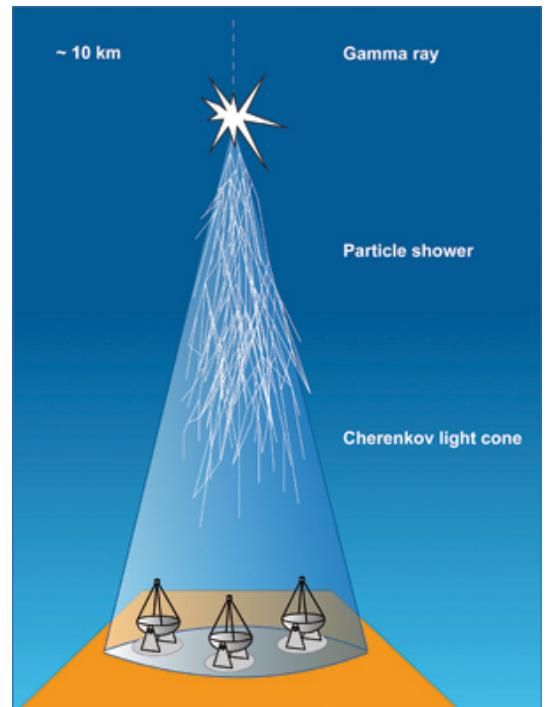


Figure 3: The cone of Cherenkov light emitted by an extensive air shower. Picture from [19]

2 Cherenkov Telescope Array

The Cherenkov Telescope Array, CTA, is a proposed ground-based observatory array of many tens of telescopes distributed over a larger energy range than before. It will allow detection of gamma rays over a large area on the ground and from multiple different directions. The array will consist of 60 - 100 telescopes of different designs and sizes to cover the aimed for energy range and area. Science goals are the understanding of cosmic rays and their role in the universe, including the study of cosmic particle accelerators, such as pulsars, pulsar wind nebulae , supernova remnants and gamma ray binaries. Secondly particle acceleration around black holes of supermassive or stellar size and lastly physics beyond the Standard Model. There are currently three groups of telescopes planed, differing in their size and achievable energy range:[3]

1. LST¹ The low energy instrument, between 20 and 200 GeV, is a 23 meter class telescope with a moderate field of view (FoV) of the order of about 4.5 degrees.
2. MST² The medium energy range, from around 100 GeV to 10 TeV, is covered by a telescope of the 12 meter class with a FoV of 7 degrees.
3. SST³ The high energy instrument, operating between a few TeV to 300 TeV, is a 4 meter telescope with a FoV ranging from 9.1 to 9.6 degrees.

There are currently two sites planed, which when deployed, will achieve full-sky coverage. The southern site in the Atacama Desert in Chile, one of the most driest and isolated regions on Earth, will consist of four LSTs, 24 MSTs, and about 70 SSTs covering an area of 4 km². The northern site will only cover 0.4 km² and will only contain four LSTs and 15 MSTs due to spacing reasons with the MAGIC observatory at the same location at the Roque de los Muchachos Observatory on La Palma , one of the Canary Islands.

— One proposed concept for the SST is the Gamma Cherenkov Telescope (GCT).... ——————
——>

There are currently 3 different prototypes in development for the SST variant: SST2M GCT

and Astri , and a single mirror prototype SST1M

This papers work is conducted on the GCT design, one of the prototypes for the high energy telescope called SST-2M GCT utilizing a 2 mirror design called Schwarzschild-Couder.

2.1 GCT

The 2 mirror design of the telescope allows us to utilize SiPMs. Current IACTs have a parabolic optical system, which is reliable and efficient but they need to be large in order to have a large

¹ LST large sized telescope

² MST medium sized telescope

³ SST small sized telescope

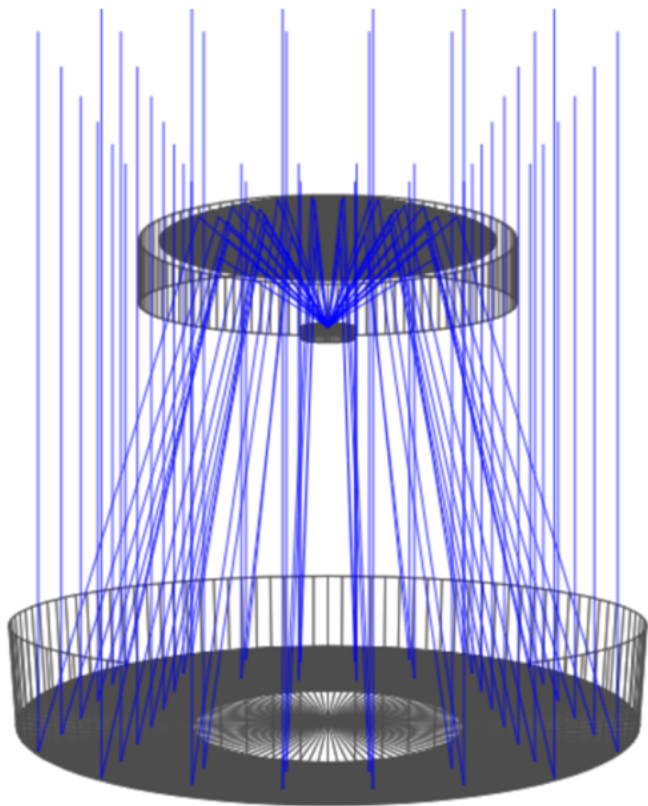


Figure 4: If possible replace picture with GCT with mounted CHEC camera picture here Picture from

223 FoV due to aberrations, resulting in huge CAMERA plate scales and therefore expensive assem-
224 bly of photodetectors.

225

226 Schwarzschild-Couder have no such aberrations, at least not on our scale, while the IACTs
227 can still have a very large Field of View (FOV) up to 15° without significant degradation of the
228 spot size. The resulting physical pixel size is more compact than that of the single mirror optics
229 and cost-effective photon sensors such as multi-anode photomultipliertubes (MAPMTs) (like in
230 CHEC-M) or Silicon Photomultipliers (SiPMs) can be used for the camera.

231 There are of course disadvantages, the optical system will be more complex, with tighter toler-
232 ances.

233

234 In summary it reduces the camera plate scale, allowing us to use SiPM photosensors.

235 2.2 CHEC-S

237 The Compact High Energy Camera, or CHEC is one of three prototype camera concepts in de-
238 velopment for one of the SST structures within CTA. One camera features 2048 SiPMs, building
239 equally many readout channels per camera. The readout is done by so called TARGET⁴ modules

⁴ TARGET TeV Array Readout with $\frac{GS}{s}$ sampling and Event Trigger

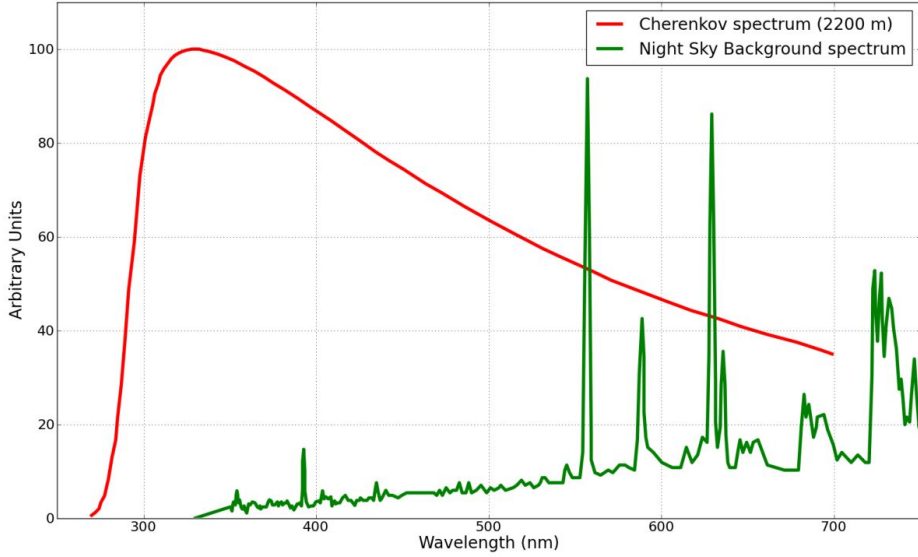


Figure 5: The spectrum of Cherenkov light observed from an extended air shower at 2200m asl. compared to the expected NSB measured in La Palma. Units on the y-axis are arbitrary because NSB and Cherenkov light vary by different parameters. Image from [10]

for sampling, digitization and triggering, one of those consists of 4 ASICs⁵ with 16 channels each. The camera houses 32 TARGET modules, one of them responsible for readout of 64 SiPMs. The TARGET modules build the front-end of the integrated electronics inside the CHEC-S camera connecting the SiPM buffer to the cameras backplane. After the SiPM is triggered the buffer amplifies the signal, that is then send to the ASIC inside the TARGET module, where an analog-to-digital converter and a shaper convert the signal before it is send to the backplane for transfer to the main array hub.

2.3 SiPM requirements for CTA

In order to make an educated choice on the best SiPM device to use to populate the cameras focal plane, an in-depth characteristic study on pulse-shape, gain, temperature-dependence, detection efficiency, thermal noise and correlated secondary effects is conducted by multiple groups within the CTA collaboration.

This paper studies noise from thermal, as well as correlated secondary effects and their temperature dependence. To be considered a promising candidate, any given SiPM device must have a high enough fill-factor (detector space versus dead space) to guarantee high Photon Detection Efficiency (PDE). This is necessary to ensure the data loss in CTA requirements? . The peak of the spectral response of the SiPM is desired to be around the spectral peak of the Cherenkov light and at the same time, must have a fast enough drop to ensure less Night Sky Background (NSB) pick up (Figure(??)). The overall noise from thermal and correlated secondary effects of the SiPM must be sufficiently below the expected NSB rate at the location (usually around

⁵ ASIC Application Specific Integrated Circuit

²⁶¹ ~20-80 MHz).

²⁶²

²⁶³ Additional?

3 Silicon Photomultipliers



Figure 6: The size of the photodetector still used in progenitor IACT experiments (PMT)(left) compared to an SiPM(right). Picture from [15]

266 Silicon Photomultipliers (SiPMs) are semiconductor photo detectors, that have attracted in-
 267 creased attention over the last decade for their possible use in astroparticle physics. The sensor
 268 consists of an array of avalanche photo-diodes, typically $50\mu\text{m}$ in size. Depending on the
 269 pixel-size, one pixel contains several 1000 diodes, hereafter called cells. Each cell is a PN junc-
 270 tion fig(7) supplied with a reverse bias-voltage above breakdown, which is called operation in
 271 Geiger-mode, in analogy to the Geiger counter. In this mode, a photon or thermal excitation will
 272 produce an electron-hole pair in the depleted region. Through impact ionization these charge
 273 carriers will in turn trigger an avalanche in a cell, which in turn generates a large output pulse
 274 typically in the range of several Mega electronvolt. This avalanche is then passively quenched
 275 by a resistor to limit the current in the substrate and to reset the cell to a quiet state so it is
 276 photosensitive again. The signal of the SiPM is the sum of the signal of all cells, read out over
 277 their quenching resistor via a common output.

278

279 Silicon Photomultipliers posses major advantages over their progenitor, the Photomultiplier-
 280 tubes, or PMT fig(??). They are more resistent to mechanical and accidental light-exposure
 281 damage through ambient light. Silicon Photomultipliers have a lower power consumption and,
 282 operating at a much lower bias-voltage, there is no need for high-voltage as in PMT. They posses
 283 a high photon detection efficiency and are insensitive to magnetic field changes. There is rapid
 284 improvement, being a fairly new technology, with new generations every ~ 5 months and de-
 285 creasing costs per mm^2 . Viewed over all cells of the whole pixel, fluctuations in the gain are very
 286 small. This is because of the uniformity during manufacture and visible in the width and the
 287 clear resolution of the p.e. peaks in the pulse area spectrum. Examples in the appendix E. Multi

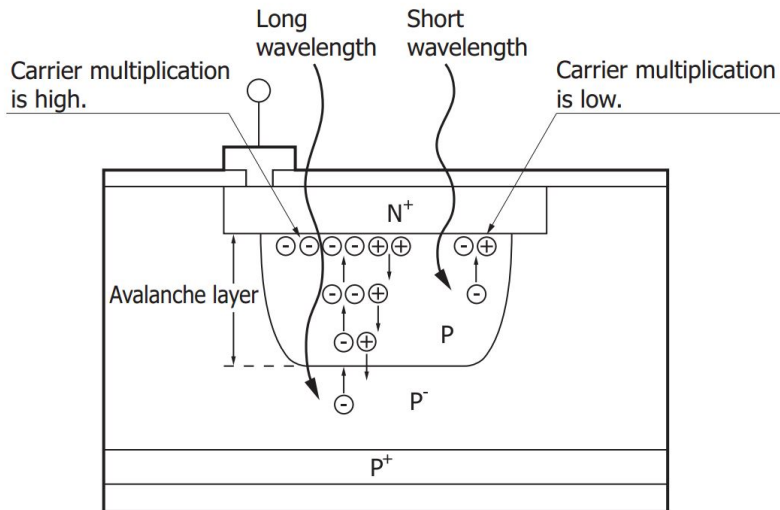


Figure 7: Structure and carrier multiplication through an avalanche inside a SiPM. Picture from [13]

288 anode photomultipliertubes do not posses those small gain fluctuations, which is due to their
 289 structure. These make Silicon Photomultipliers an interesting candidate in astrophysics experi-
 290 ments for both, space- and ground-based telescopes (or IACTs, Imaging Atmospheric Cherenkov
 291 Telescopes).

- 292 1. Sturdiness
- 293 2. May be exposed to ambient light (observation during bright moonlight periods possible)
- 294 3. Low power consumption ($\leq 50\mu\text{W}/\text{mm}^2$)
- 295 4. Low operation voltage (typically $\sim 20 - 100$ Volts)
- 296 5. No need for HV, as in PMTs
- 297 6. High Photon detection efficiency
- 298 7. Insensitivity to magnetic fields
- 299 8. Being a fairly new technology it is steadily improved, meaning a new generation of SiPMs
 300 every 5months
- 301 9. Rapidly decreasing cost per mm^2

302 The currently most challenging astrophysics experiment Silicon Photomultipliers are consid-
 303 ered for is use in Cherenkov telescopes, with very demanding expectations in terms of photon
 304 detection efficiency. The photon detection efficiency quantifies the absolute efficiency of any
 305 photon detector to absorb a photon and produce a measurable signal at its output. To achieve

306 a high photon detection efficiency in the 450nm regime, the design moves to very thin im-
 307 plantation layers on the surface in order to minimize the absorption of shorter wavelength pho-
 308 tons in insensitive areas. Figure(??) Different entry window coatings and avalanche structures
 309 (trenches etc.) explore the capable enhancements in the blue sensitive UV region.

310 3.1 Gain of a Silicon Photomultiplier

312 The gain of a Silicon Photomultiplier measures the internal conversion of a photon incident into
 313 a signal at the output. The amplification of the device is expressed as the average number of
 314 charge carriers produced. There is no distinction whether the incident was caused by a single
 original photon or a thermal electron.

$$M = \frac{Q}{e} \quad (1)$$

$$Q = C * (V_{bias} - V_{breakdown})$$

Figure 8: The gain (M) of a Silicon Photomultiplier results from the deposited charge (Q) of the pulse generated from one cell when it detects one photon, divided by the charge per electron (e). The charge deposited per event is proportional to the cell's capacitance (C) and the supplied over-voltage ($V_{bias} - V_{breakdown}$). This results in the gain (M) in units of total number of charge carriers, usually in the several 10^6 range.

315
 316 Estimation can be done via the voltage mean of the 1 p.e. amplitude: (e.g. see Figure (25)). For
 317 a better understanding, stating the gain in units of mV per photoelectron or $\frac{mV}{p.e.}$ is more suitable,
 318 as it gives a direct correlation between detected photoelectron and expected voltage amplitude.
 319 Given the very narrow pulse shapes, using the average pulse amplitude and extracting FWHM
 as a time measure of the total charge flowing during discharge and using the formula:

$$Q(p.e.) = C * (V_{bias} - V_{breakdown}) \quad (2)$$

$$U(p.e.) = \frac{Q(p.e.)}{t(FWHM)} * 50\text{ohm}$$

Figure 9: Resulting in the expected event charge flowing during capacitor discharge. Given the bias-voltage and C as capacitance of one cell and the resistance of the quenching resistor, a conversion factor and the average amplitude per photoelectron can be extracted.

320
 321 The gain is obviously higher the larger the cell capacitance or the higher the bias-voltage (eq 1)
 322 will be. But increasing the bias-voltage also increases dark counts and crosstalk. The gain is also

dependent on the temperature, mainly through the quenching resistor but also from the silicon bulk itself, at a certain bias-voltage decreasing as temperature rises. The quenching resistor is affected by a lowering of the electrical conductivity with rising temperature, in accordance to the Wiedemann-Franz law, stating that the ratio of electrical and thermal conductivity remains constant. The silicon bulk at rising temperatures underlies increased crystal lattice movement. This impinges charge transport by increasing the probability that carriers might impact on the lattice before the carrier energy has become large enough for continued ionization. In order to counteract this, the electric field must be increased by increasing the supplied bias-voltage so ionization is more likely. Doing this has drawbacks as discussed before. For application as a photon detector, keeping the gain constant is an inevitable step, otherwise the shifting gain leads to problems. To do that, either the bias-voltage need to be adjusted to match ambient temperature, leading to problems with varying dark counts and crosstalk. Or the surface temperature must be regulated to be kept constant. Although more challenging hardware would be required, the latter option has obvious advantages, keeping dark counts and crosstalk and more important the gain constant by simply regulating the surface temperature.

Taking into account equation 1, it appears that the breakdown-voltage can be estimated from the zero-crossing of a linear extrapolation of the gain at every bias-voltage per temperature. By doing this a linear breakdown-voltage dependence of the temperature can be observed. Appendix Figure(53)

I note that the gain, when parametrized over over-voltage, is essentially temperature independent, as I will show later in chapter 6: Figures (31) , (36) , (41) , (44)

344

345 3.2 Thermally induced dark counts 346

Still temp dependent when plotted vs overvoltage Inside the Silicon Photomultipliers depleted region a dark pulse originates from thermal excitation of an electron to the conduction band. Without an event photon present to trigger the avalanche, it is still indistinguishable from a photoelectron pulse. These thermally generated carriers are observed along with the signal from a real photoelectron, presenting an irreducible source of noise. The number of dark pulses observed is referred to as dark counts and the number per second as the dark count rate. For applications that need to operate in an environment with low noise, those dark counts are a concern. In IACT application of Silicon Photomultipliers however, this is only a minor problem, since IACTs operate in a naturally noisy environment. Even though sky darkness is one of the prime criteria of the proposed site selections for CTA, the surrounding Night Sky Background (NSB) at the most darkest side in Namibia will still exceed any random noise in the detector. The pollution of those NSB photons is unavoidable noise and will essentially limit the low energy resolution of the telescope to the NSB rate. As long as any random noise, being dark counts or other, is significantly below the NSB rate, it will not affect the telescopes performance.

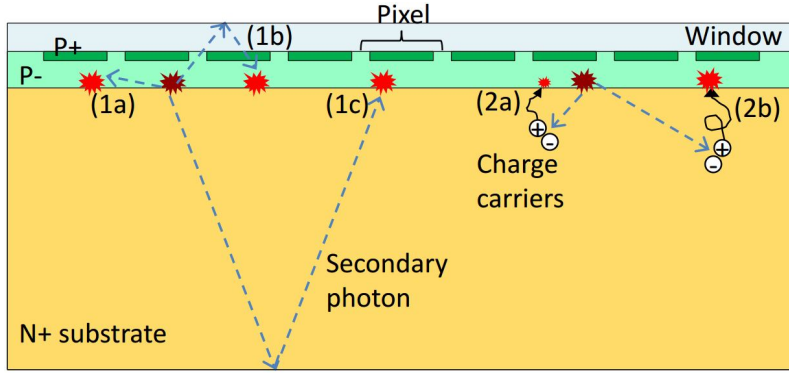


Figure 10: Secondary effects (bright red) caused by primary avalanches (dark red) in a Silicon Photomultiplier. In this paper a single pixel, in this figure, is referred to as a cell (see 3). Everything labeled under 1 is associated with prompt cross-talk, afterpulsing labeled as 2a, and delayed cross-talk labeled as 2b. Image adapted from [11]

361 Telescope performance simulations of the Schwarzschild-Couder MST of CTA at the site of
 362 Namibia showed a rate of $\sim 20 - 80$ MHz per pixel for one of the older SiPM iterations
 363 from Hamamatsu. [10] This is purely for NSB photons and pixels with a size of $6 \times 6 \text{ mm}^2$,
 364 the covered range originates from differences in illumination level of the night sky by galactic-
 365 and extragalactic-fields. I note that the DCR, when parametrized over over-voltage, remains
 366 temperature dependent, as I will show later in chapter 6: Figures (32) , (37) , (42) , (45)

367

368 3.3 Avalanche-induced secondary effects

369 An avalanche originating from the primary cell can sometimes, either directly or by reflection,
 370 propagate outside the cell and trigger an avalanche almost simultaneously in a secondary cell.
 371 This will, unless accounted for, degrade the Silicon Photomultipliers photon counting resolution,
 372 since the signal will be a merge of cross-talk cells and real incident cells. The probability for this
 373 is referred to as the cross-talk probability and the effect as the Optical Cross Talk, since it is con-
 374veyed via secondary photons generated in the primary avalanche. Afterpulsing also falls under
 375 this category, with the main difference to cross-talk being that the carrier triggers a secondary
 376 avalanche in the primary cell, basically generating a parasitic pulse inside the previously fired
 377 cell. Contained in a single cell, afterpulsing increases the measured charge registered for an in-
 378 cident photon. The difference in arrival time of the secondary avalanche distinguishes different
 379 components comprising the cross-talk and afterpulsing. Those secondary avalanches can again
 380 emit photons, that can trigger secondary avalanches themselves, leading to high amplitudes,
 381 even in dark conditions.

382 Figure (10) shows different physical processes causing secondary effects in Silicon Photomulti-
 383 pliers based on their delay time. Cause of the delay time is the dependence on the penetration
 384 depth of the incident photon, or the region the dark count generated, and the diffusion time

386 inside the substrate. At long delay times afterpulsing and cross-talk are not distinguishable.
387 The prompt Optical Cross Talk happens basically simultaneous to the primary avalanche, since
388 it is unaffected by the primary cells recovery time and is labeled 1 in Figure (10). It is either
389 triggered by the secondary photon directly (1a) reaching the neighboring cell, or after first re-
390 flecting on the surface layer (1b) or the bottom surface (1c). If the cross-talk avalanche delay
391 time is shorter than the detection resolution, the difference in signal between an Optical Cross
392 Talk event or an incident photon being detected, is not observable.
393 Time delayed Optical Cross Talk is caused by a carrier generated in the non-depleted substrate
394 diffusing to a neighboring cell and triggering an avalanche in the depleted region (2b). If the
395 carrier stays in the primary cell, the triggered avalanche is labeled afterpulsing (2a) and will
396 have a lower amplitude, due to the cell not being recovered yet. The delay time is influenced
397 by how deep the carriers are being trapped in the substrate, the time they need to diffuse to the
398 surface, and also distinguished by traps with different lifetimes.
399 This is very important in IACT performance, since this effect gives random NSB and dark count
400 photons the ability to rise to arbitrarily large amplitudes. The consequent need to raise the
401 trigger threshold to counteract the resulting rising accidental-triggerate has a negative impact
402 on the low energy resolution of the telescope.
403 Parametrized with over-voltage, the secondary avalanche effects are temperature independent,
404 shown in chapter 6: Figures (33) , (38) , (42) , (45)

405

406 3.4 OCT dependency on cellsize

408 Cross-talk is dependent on the ability of the secondary photons to reach a neighboring cell. This
409 means, that an increase in cell-size and therefore cell-area should directly correlate with the
410 Optical Cross Talk of a pixel. In Figure (11) the results of the complete Optical Cross Talk of 2
411 sets of $50\mu\text{m}$ and $25\mu\text{m}$ HPK S13360 devices are shown. Plotting the results of 2 similar devices,
412 only different in their cell-size, and then multiplying the $25\mu\text{m}$ results by the factor derived
413 from their difference in area, here 4, a correlation is visible. Scaling up the Optical Cross Talk
414 of the $25\mu\text{m}$ cell, shows an overlap between the 2 cell-sized pixels. This means, that the Opti-
415 cal Cross Talk is directly area and therefore cell-size dependent. Research by J. Rosado and S.
416 Hidalgo [11] on the cross-talk probability of Hamamatsu SiPMs showed through Monte Carlo
417 simulation, that the prompt crosstalk mostly takes place in a small area of pixels (~ 8) around
418 the primary one. Which means, that the cross-talk is directly increasing with increasing cell-size,
419 or in other words: with chance to diffuse to a neighboring cell. Small cells reduce the chance,
420 as there is less area to a neighboring cell to pass through.
421 Since the measurements conducted by me do not differ between the range of secondary
422 avalanche effects, the Optical Cross Talk shown contains every aspect, prompt and delayed
423 as well as afterpulsing.

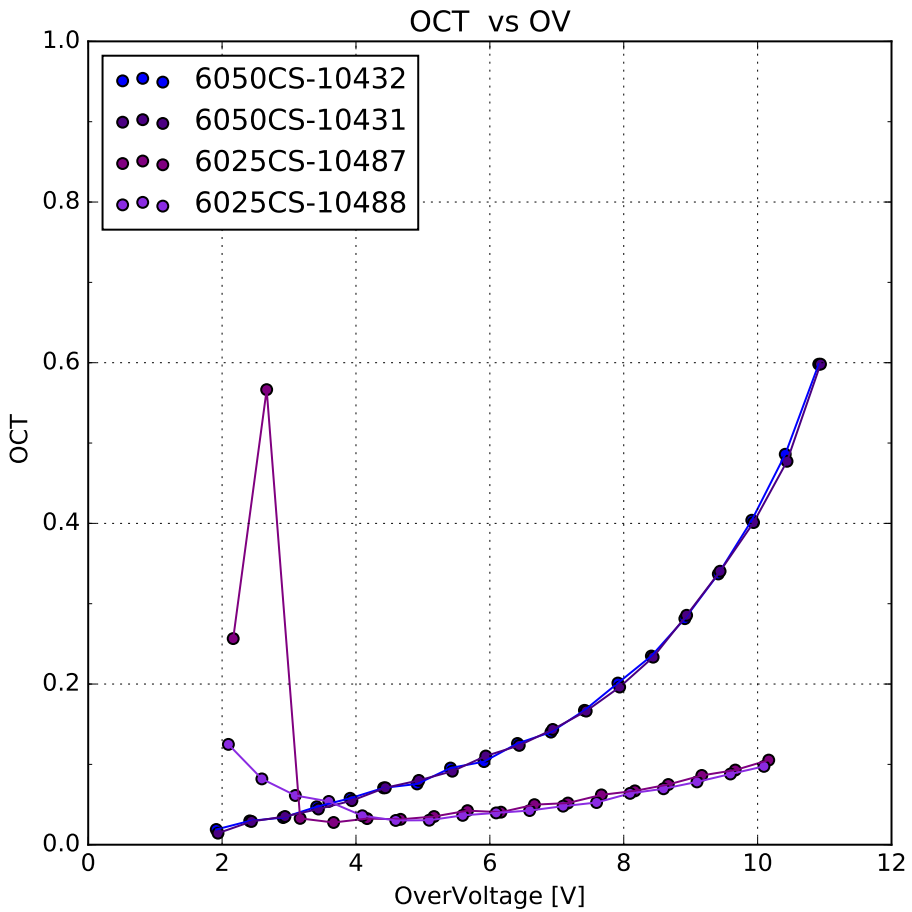


Figure 11: Results of the Optical Cross Talk of 2 sets of 2 similar HPK S13360 devices, that only differ in their respective cell-size. HPK S13360 is the first device incorporating physical trenches in the upper layer, optically isolating each cell. Consequence to this is a drastic reduction in prompt cross-talk. Delayed cross-talk and afterpulsing are basically unaffected. Upscaling the 25 μ m results shows an overlap between the 2, see text.

424 3.5 Photon Detection Efficiency

425 The Photon Detection Efficiency is the probability of a detector to absorb an incoming photon
 426 and produce a measurable signal at its output, and depends on a number of factors. First the
 427 photon must enter the depleted region via transmission through the surface of bare silicon,
 428 which has a reflectivity of 30%. However, the transmission probability can be improved by
 429 coating the surface with a substrate with adequate thickness and a refraction index between
 430 air $\eta_{air} = 1$. and silicon $\eta_{silicon} = 3.4$. Devices presented in this paper are coated with epoxy,
 431 a silicon resin and glass. The coating also has the added benefit of insulating and protecting
 432 the cells against environmental influence. A possible negative effect of coating is an increase in
 433 prompt cross-talk and a larger dependency of the overall cross-talk on the cellsize. The second
 434 factor is quantum efficiency, describing how susceptible the depleted region is to photons ex-
 435 citing electrons from the valence band to the conduction band. This is sometimes referred to as
 436

437 spectral response of a detector to reflect the wavelength dependence of a detector and makes
438 the PDE wavelength dependent. The over-voltage dependency of the PDE is conveyed by the
439 third factor, the avalanche probability. It depends on the electric field present, and thus on the
440 applied over-voltage. The last factor is the fill-factor: the more the surface area of the detector
441 is covered with active-area cells and the less dead-area exists between cells the higher the fill-
442 factor is.

443 The Photon Detection Efficiency is commonly measured by illumination of the pixel and a cali-
444 brated reference photodiode with a flashing light source, and determining the average number
445 of photons hitting the photosensor during a light pulse.

$$PDE = \frac{N_{\text{detected photons}}}{N_{\text{total photons}}} \quad (3)$$

Figure 12: Photon Detection Efficiency is the percentage of detected photons versus overall emitted photons.

4 Experimental Setup

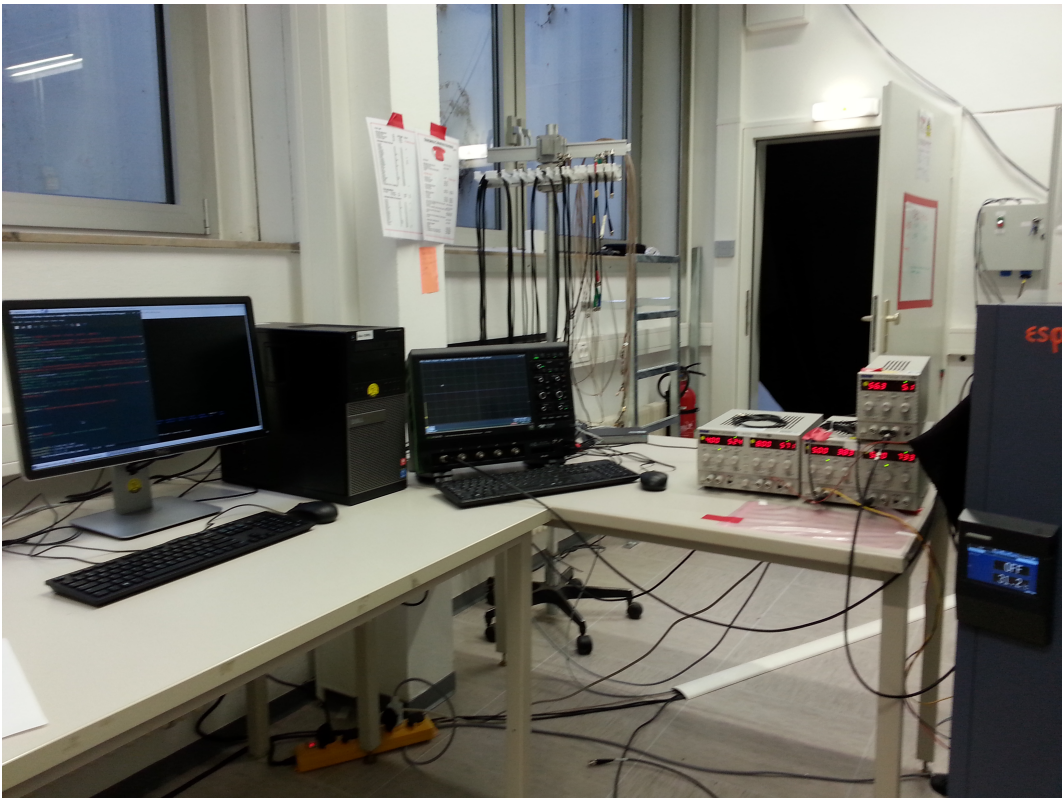


Figure 13: Will be updated. With Alphabetical captions for the different steps and references later in the text and setup scheme below, Picture of the inside of the thermal chamber is missing, will do later, and try to fit it next to this one

448 The experimental setup in general is designed to house a variety of SiPM devices. Over the
 449 course of this paper, 5 different types of SiPMs were mounted on the setup and evaluated. It
 450 involves a thermal chamber Figure(14)(A) for temperature regulation which proved light tight
 451 and thus also serves as a dark box, to prevent any stray light to reach the SiPMs surface. De-
 452 pending if the SiPM Figure(14)(A1) in testing is pre-manufactured on a test-array or supplied as
 453 a standalone chip, it is either mounted directly on a mechanical arm inside the chamber in the
 454 former case, or in the latter the mechanical arm supports a specifically designed PCB connecting
 455 to the device. Via the mount, bias-voltage is supplied and signal is transferred to the shaper
 456 Figure(14)(A2). !!!!!Need some more details on shaper

457

458 In some cases the output signals amplitude is too low to trigger the oscilloscope, therefore
 459 amplification is needed. I used an amplifier from MiniCircuits ZFL-1000-LN+ SN:283401542
 460 Figure(14)(A3) supplied with different voltages depending on the tested device to amplify the
 461 shaped signal.

462

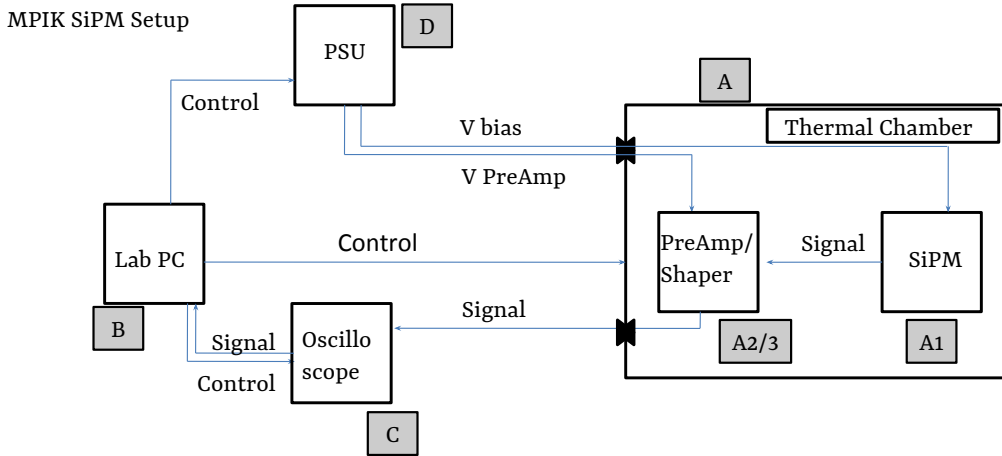


Figure 14: Experimental setup scheme, Annotations see text

463 Data acquisition in the Laboratory is realized by a Lab-PC Figure(14)(B) , that forms the
 464 central control station for multiple pieces of equipment. It is connected to the oscilloscope
 465 Figure(14)(C), which records the waveforms of the device in testing, and then sends the data
 466 back to the PC via ethernet. The oscilloscope is a Lecroy XXXXX SN capable of $2.5 \frac{GS}{s}$. The
 467 power supplies Figure(14)(D) control the bias-voltage of the Silicon Photomultipliers, ramping
 468 of the bias-voltage is controled by the PC. Lastly the thermal chamber is connected to the Lab-
 469 PC, which controls the temperature, and continuously rechecks it during temperature ramps.
 470 Signal transfer from the shaper to the oscilloscope is via a throughput on the side. All equip-
 471 ment is connected via ethernet, plugged into a common hub, to form a local network. While
 472 the temperature of the thermal chamber is ramping from the previous to the next set-point, the
 473 data is send to the Lab-PC.

474

475

476 Temperature regulation is an issue in the teststand, as there is no way of controlling the
 477 SiPMs surface temperature. In dark conditions however, without conducting illumination tests,
 478 the shift in temperature on the SiPMs surface is only minimal. (Find the breakdown-voltage
 479 dependence on temperature in the appendix (??)). Checking the surface temperature of all
 480 devices with a temperature probe during testing showed minimal rising temperatures. So the
 481 influence of the temperature on the breakdown-voltage is only of minor concern. However,
 482 once illumination tests begin, the rising temperature on the SiPMs surface will no longer be
 483 negligible and the temperature must be regulated, either by cooling of the surface or including
 484 the temparature parameter.

485 5 Data Analysis

487 The analysis of the Silicon Photomultiplier waveforms is done exclusively in python following
488 the sequence:

489 (Possibly to much detail in here)

- 490 1. data conversion
491 2. pedestal subtraction
492 3. peak detection
493 4. gain extraction
494 5. calculation

495 The waveform data, after being transferred to a separate PC, is analyzed offline. The goal is
496 to extract event-data from the waveforms in order to produce pulse-area spectra for every bias-
497 voltage at every temperature. To that end, the pedestal of the electronic noise must be found and
498 subtracted from the data. After that, event-pulses are detected and integrated. This generates
499 a list of pulse-areas, which is in turn used to fill a pulse-area histogram. To this pulse-area
500 histogram, a model is fitted from which the gain can be extracted. Due to the linear behavior
501 of the gain with rising bias-voltage, a regression line is fitted, from which the Dark Count Rate
502 and the Optical Cross Talk are calculated using the original pulse-area histogram.

503 5.1 Tracefile Conversion

505 The oscilloscope produces the waveform data in its intrinsic data format, called a trace with
506 the data suffix trc in binary. A trace file contains a header and two binary lists, an amplitude
507 based on the oscilloscope's voltage-range and offset, and a list of the same length containing the
508 associated event-time, based on the time-range and horizontal offset. The first step is therefore
509 a conversion of the amplitude and associated event-time of all segments of a waveform trace
510 file into two lists of floats.

511 5.2 Pedestal Subtraction

513 A single waveform from the oscilloscope is
514 anticipated to be uncentered fig(15)(grey), it
515 will be slightly above or below zero, depending
516 on the device setup (some devices pro-
517 duce inverted signals). The signal is mixed
518 with electronic noise when it is observed
519 and forms a pedestal, shifting the mean of
520 the waveform from its original position to
521 zero. Pedestal subtraction removes this av-
522 erage noise.

523 The first step of the process is reading in the
524 uncentered waveform fig(15)(grey) and cal-
525 culating an initial mean(mean0), expected to
526 be slightly higher than the actual mean of the
527 noise, due to the presence of event-pulses.
528 The waveform is then shifted to about zero,
529 by subtracting the mean0. A second mean of the now nearly centered waveform is taken
530 (mean1). Now a new, same-sized array is formed and filled with the data from the wave-
531 form that is smaller than mean1, this represents the negative part of the noise. The data larger
532 than mean1, the positive noise, is also filled into the array, but is negative-signed. This cre-
533 ates an array of the waveform centered around zero and, above the mean1, folded towards the
534 negative. It proved reliably, that calculating the root-mean-square of this helper-array is a solid
535 possibility of stripping the waveform of event-peaks. Taking the root-mean-square with a factor
536 3 of the helper-array, a cut is now applied to the waveform on both, the positive and negative
537 side. In that fashion, the remnant is the waveform between the positive and the negative root-
538 mean-square and is now called a peakless-signal, representing the noise of the waveform.
539 Pedestal subtraction is done by calculating the mean of this peakless signal and subtracting
540 it from the waveform. After that, the peakless signal is also smoothed by convolving it with
541 a wide-windowed gaussian and subtracted from the waveform to eliminate any slow moving
542 noise, the resulting waveform is called "Filtered Signal 1" fig(15)(blue).

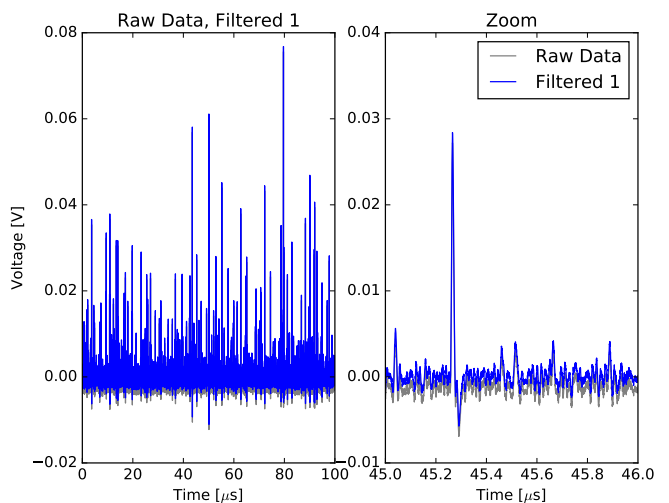


Figure 15: Raw, real data from a HPK SiPM in grey, in blue the pedestal subtracted and smoothed "Filtered Signal 1"

543
544

5.3 Peak Detection

545 Peak detection exploits the fact, that the first
546 derivative of an event-peak will cross zero
547 into the negative at the time of the peak max-
548 imum. The presence of random noise in the
549 signal however will lead to many false de-
550 tections. Therefore, before the detection of
551 the event-peaks, the waveform fig(16)(grey)
552 is smoothed with a narrow-window gaussian
553 with a width of about the FWHM of the de-
554 vices characteristic event-pulse, in order to at-
555 tenuate non-event peaks fig(16)(blue). After
556 the first derivative of the signal is calculated,
557 which in python is a fast process if using ar-
558 rays, a number of parameters decide the va-
559 lidity of the detected peaks. Most important
560 parameters are a certain predetermined mini-
561 mum amplitude, called the amplitude thresh-
562 old or: minimum peak height. This is right now determined by eye, but could later be calculated
563 based on the noise level. The second important parameter defining validity is the minimum peak
564 distance, which defines how close two events can occur after another. The value is determined
565 by the FWHM of the device in testing, which I expect to be sensible enough to resolve two events
566 happening close after another. The peak detection algorithm can not distinguish between in-
567 stantanious and delayed Oprical Cross Talk, but nonetheless, due to the fact, that the signal data
568 is taken over many micro-seconds, all events are detected, independent of their source. On the
569 other hand, this also means, that it is possible for two events to happen at the same time, for
570 example a real photoelectron-event coinciding with delayed Optical Cross Talk. This can not be
571 distinguished and will lead to a slight shift of the amplitude. (because delOCT is partial 1p.e.)

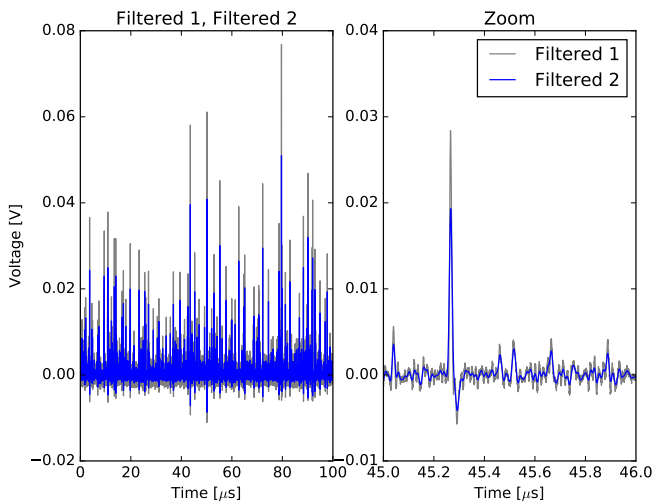


Figure 16: "Filtered Signal 1" in grey before smoothing with a narrow gaussian to generate "Filtered Signal 2" in blue, which is used for peak finding.

5.4 Gain Extraction

574 The detected peaks are integrated with a window
 575 extending symmetrally from the peak maximum,
 576 the width is chosen as slightly wider than the
 577 peaks FWHM. The generated list of peak areas is
 578 generating a peak area histogram, which is fitted
 579 with multiple gaussians using iMinuit in python ,
 580 seen in Figure (17). Two parameters are extracted
 581 from the fit to the peak area histogram. The first,
 582 the position of the 1p.e. peak is the position of the
 583 maximum of the first peak in the histogram, and
 584 the position of corresponding multiple p.e. events
 585 should be integral factors of the 1p.e. position.
 586 This proved to not be the case for some devices,
 587 the suspected source of this error is a pedestal
 588 generated during the peak integration. I studied
 589 the effect of the integration window in more de-
 590 tail in chapter 5.5.1.

591

592 A second parameter is extracted from the peak
 593 area histogram to deal with this problem, which is
 594 the distance between N p.e. peak maxima of the
 595 histogram, labeled $\Delta p.e.$, which defines the gain.
 596 The apparent pedestal of the pulse area histogram
 597 makes extraction of the two parameters necessary
 598 in order to calculate the Dark Count Rate and the
 599 Optical Cross Talk. The gain of a Silicon Photo-
 600 multiplier has a linear dependence of the supplied
 601 bias-voltage. Given that the bias-voltage range
 602 is deliberately chosen such that the over-voltage
 603 ranges from about 1V growing upwards, the range
 604 of linearity only starts at around the point of op-
 605 eration given by the manufacturer of the device.
 606 At the higher end of the bias-voltage range the be-
 607 haviour usually starts to divert from the linearity.
 608 In order to get an estimation of the gain over a
 609 large range, both previously extracted parameters, the 1p.e. peak and the distance $\Delta p.e.$ are

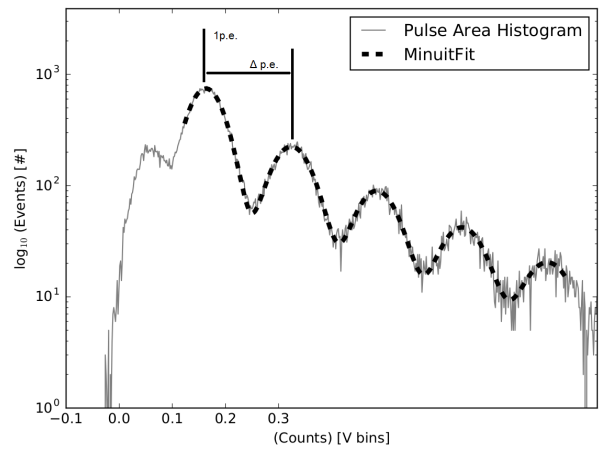


Figure 17: Pulse Area Histogram of a HPK S12642 with 1p.e. and $\Delta p.e.$ positions. Multi gaussian as black dashed line.

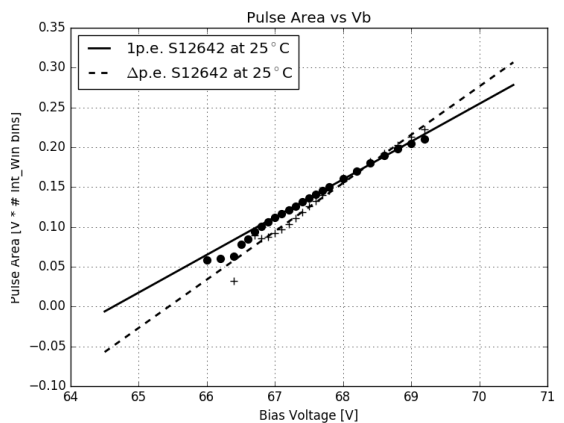


Figure 18: 1p.e. position and $\Delta p.e.$ extracted from the Pulse Area histogram at every bias-voltage for HPK S12642 with their respective regression lines.

fitted with a linear regression line. The fit assumes linearity utilizing weighted least squares inherited from pythons statsmodels package. For the fit, only the data, where at least 3 gaussians are fitted to the peak area histogram is taken into account. Plotting both extracted parameters, as well as their respective regression lines versus bias-voltage, as in Figure (18), shows the difference between the two parameters. (SHOW FOR ALL DEVICES IN APPENDIX???). Comparing the manufacturer supplied breakdown-voltage from the datasheet for all devices showed, that the zero-crossing of the 1p.e. regression line is more consistent with datasheet values, in contrast to the zero-crossing of Δ p.e., which lies slightly higher. The over-voltage, corresponding to the set bias-voltage at any given temperature is calculated from this breakdown-voltage. Dark Count Rate and Optical Cross Talk are calculated utilizing 1p.e. position and Δ p.e. derived from the regression line. Both values are applied, in the calculation, to the peak area histogramm with the Dark Count Rate being defined as:

$$DCR = \frac{N_{events(>0.5p.e.)}}{T_{experiment}} \quad (4)$$

Figure 19: The Dark Count Rate of a Silicon Photomultiplier is defined as all events exceeding 0.5 p.e. in amplitude $N_{events(>0.5p.e.)}$ occurring over the experiment time $T_{experiment}$. Included in the measurement are thermally generated dark counts, as well as delayed cross-talk and afterpulsing with only a minor contribution.

, and the Optical Cross Talk as:

$$OCT = \frac{N_{events(>1.5p.e.)}}{N_{events(>0.5p.e.)}}. \quad (5)$$

Figure 20: The Optical Cross Talk of a Silicon Photomultiplier is defined as all events exceeding 1.5 p.e. in amplitude [$N_{events(>1.5p.e.)}$] devided by all events exceeding 0.5 p.e. in amplitude [$N_{events(>0.5p.e.)}$]. It scales with the number of photons produced inside an avalanche, as well as the probability of these photons to trigger a neighboring cell

623
624

5.5 Data Challenges

625
626

5.5.1 The influence of the minimum peak distance

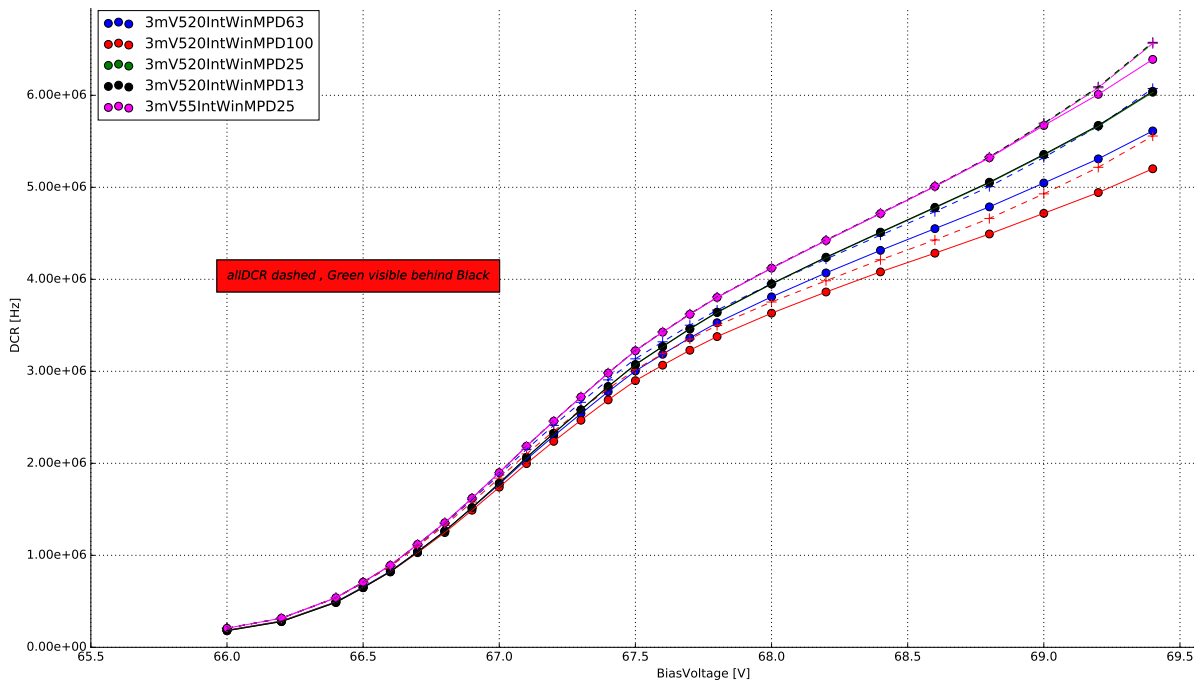


Figure 21: The difference between 4 minimum peak distance windows, in time-bins, during the peak detection. The dashed lines are the Dark Count Rates considering all recorded events, forming an upper limit. In pink, the effect of a different integration window is shown.

627 The influence of the minimum peak distance is shown in Figure (21) . Based on their bin-
628 width, four different windows are tested. With the oscilloscopes sampling rate of $2.5 \frac{GS}{s}$, the
629 windows of 100, 63, 25 and 13 time-bins, correspond to 40, 25, 10, 5 ns windows respectively.
630 With a event pulse FWHM of 10ns, setting the minimum peak distance to 100 bins, resulting
631 in a 40ns window is visibly to large, as the algorithm will skip over valid data Figure (21)(red).
632 After an event is detected, skipping over 40ns worth of data will result in errors of the Dark
633 Count Rate, since the calculation uses the complete experiment time. Therefore a more reliable
634 distance window must be chosen. The second window of 25ns was the next approach, origi-
635 nating from the length of the pulse-tail fig(21)(blue). This would lead to no detected events
636 overlapping with the tail of one previously detected, resulting in a sharper pulse-area spectrum.
637 Compared to a window of approximately the pulse FWHM, the previously discussed window
638 would still lead to lost event-data. Since the sharpness of the pulse-area spectrum is already
639 sufficient, a window around the pulse FWHM was chosen as reference for all measured de-
640 vices Figure (21)(green). Going lower than the pulse FWHM showed no improvement Figure
641 (21)(black).

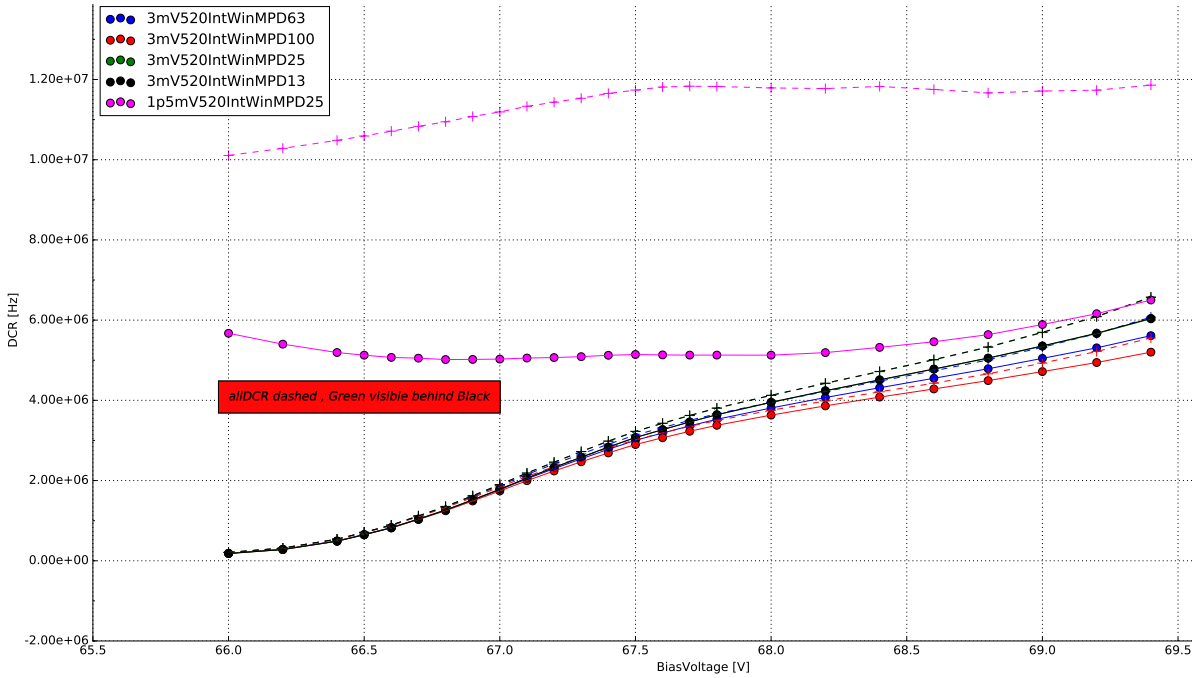


Figure 22: The difference between 4 minimum peak distance windows, in time-bins, during the peak detection. The dashed lines are the Dark Count Rates considering all recorded events, forming an upper limit. In pink, the effect of a lowered peak detection threshold is shown.

642 5.5.2 The influence of the integration window 643

644 Figure (21) also shows the influence of the size and shape of the integration window on the Dark
645 Count Rate. The influence of the chosen integration window is most visible in their respective
646 pulse area spectra. Choosing a narrow, symmetrical integration window of 5ns left and right of
647 the peak maxima, the noise peak, or zero-peak, is much more prominent compared to the pulse
648 area spectrum of a symmetrical 10 ns window. This leads to errors in the multi-gaus fitting
649 step, or the fitting will fail altogether. An asymmetrical integration window of 5ns left, 20ns
650 right, to capture the influence of the pulse-tail proved, at first, to be the best solution as their
651 was no visible zero-peak present. The low amplitude pulses are averaged out by the extended
652 integration window to the right of the pulse-maximum. The downside of the asymmetrical
653 window is the shifting of the pulsle area spectrum and the fact, that the N p.e. peaks get
654 blurred. The next step was widening the window on both sides. This proved the best solution,
655 since there is no zero-peak visible and the N p.e. peaks are gaussian shaped. Please see the
656 Appendix for the respective plots of pulse area spectra of the different windows C.

657 5.5.3 The influence of the peak detection threshold 658

659 Choosing an adequate peak-finding threshold is a crucial step. Lowering of the threshold to
660 ~ 0.5 p.e. will cause the peak finding algorithm to misinterpret a lot of noise peaks as actual

661 dark incidents. This, of course, leads to errors in the gain extraction and even if a gain regression
662 line can be extracted, the resulting Dark Count Rates and Optical Cross Talk will be incorrect.
663 Figure (22), shows the effect a low peak finding threshold has on the Dark Count Rate.

6 Results

6.1 SiPM devices for CTA

Manufacturer	pixel size	cell size	coating	connection	specifics	pre-Amp
HPK S12642-1616PA-50 *CHEC-S SiPM	3mm^2	$50\mu\text{m}$	SR	TSV	no trenches	CHEC-S buffer
HPK LCT5 S13360-6050CS	6mm^2	$50\mu\text{m}$	SR	wire-bonds	trenches	MS 13V
HPK LCT5 XXXXXXXXX	6.915mm^2	$75\mu\text{m}$	SR	wire-bonds	trenches	MS 8V
HPK 6050HWB-LVR-LCT	6mm^2	$50\mu\text{m}$	SR	TSV	trenches	MS 13V
SensL FJ60035	6mm^2	$35\mu\text{m}$	glass	TSV	no trenches	MS 15V

Figure 23: List of SiPM devices which results are presented in this paper. *(SR: silicon resin , MS: MiniCircuits , TSV: through silicon via)

668 Silicon Photomultiplier devices for CTA are researched by many different groups, validating
669 different characteristics. Besides the current SiPM for CHEC-S, newly developed prototypes of-
670 fer a diverse range of pixel- and cellsizes. The majority of the devices are tested in Japan, at
671 the University of Nagoya, conducting in depth analysis of the characteristics over a wide over-
672 voltage range at one static temperature, mainly focusing on PDE and OCT, and their correlation.
673 This correlation of OCT and PDE for all devices determines the candidate for CHEC-S, by com-
674 paring the highest PDE at the lowest possible OCT for each device. At MPIK, chosen candidate
675 devices are examined regarding their temperature dependence and as to assist in the final deci-
676 sion by confirming results with a different analysis technique.

677 The chosen devices include the current CHEC-S device HPK S12642-1616PA-50, from Hama-
678 matsu Photonics K.K., to be implemented in the first prototype camera. It is a previous gener-
679 ation SiPM, which was decided for use in 2014.(, due to the limited availability in high PDE
680 devices at that time.) The manufacturer supplies a 16*16 channel premounted tile of 3mm^2
681 pixels with a cell-size of $50\mu\text{m}$. To emulate the usage in a TARGET module, 4 3mm^2 pixels are
682 electrically connected to form a 6mm^2 superpixel. The tile is typically coated with epoxy resin,
683 but due to specific requirements regarding the uniformity of the coating, it was replaced with
684 a very thin layer of silicon resin equivalent to later prototypes. The CHEC-S devices electroni-
685 cal connection is realised via the new through-silicon-via (TSV) concept of running a connecting
686 solder through the silicon bulk, instead of wiring on the outside, greatly increasing the fill-factor,
687 but also including some disadvantageous sideeffects later shown.

688 Additional tested devices include the LCT5 generation from Hamamatsu Photonics K.K., so
689 called due to their low cross talk properties, namely the commercial available S13360-5050CS.
690 This device is the first to include physical trenches between the cells, effectively dividing the
691 cells optically and thus reducing prompt cross-talk probability.
692 The LCT5 generation also made two prototype devices available for testing at MPIK, the first,
693 HPK LCT5 SN CATANIA, is a larger iteration with a cellsize of $75\mu\text{m}$ and a pixelsize of 6.915mm^2 .
694 Being from the LCT5 generation it also includes optical trenches. The second device available
695 is a LCT5 prototype designated 6050HWB-LVR-LCT , LVR meaning low-voltage-range, with the
696 same physical dimensions and properties as the S13360 device but incorporating TSV technology
697 and possibly other unknown deviations.
698 The final device is a commercially available test-array designated FJ60035 from SensL, pre-
699 mounted on a test-array by the manufacturer. It has the same pixel-size, but a much smaller
700 cell-size $35\mu\text{m}$ than the previous mentioned devices and a different coating (glass).

701

702 The tests conducted in Nagoya contain many different iterations of the LCT5 generation with
703 varying pixel- and cell-sizes.

704 For a full overview of the considered Silicon Photomultipliers, please refer to the appendix under
705 (??).

706

707 6.2 Hamamatsu S12642-1616PA-50 50 μ m 3mm

708 The Silicon Photomultiplier by Hamamatsu Photonics designated
709 S12642-1616PA-50 is a 3 mm by 3 mm device. The array uses
710 the through-silicon-via technology, meaning there are no wire-
711 bonds present, the electrical connection is realised through the
712 silicon-body. The pixels are coated with a thin film of silicon
713 resin, after the previously used epoxy resin proved not uniform
714 enough. One array consists of 256 pixels, 4 of which are elec-
715 trically tied together to form a 6mm by 6mm superpixel respec-
716 tively. This practice is necessary for the pre-production camera
717 CHEC-S, because the focal plane is mechanically designed to house 64 6mm² pixels, connected
718 to the TARGET modules. Furthermore I expect this to have an influence on my results due to
719 electrical crosstalk, but this is only of minor concern due to the following.

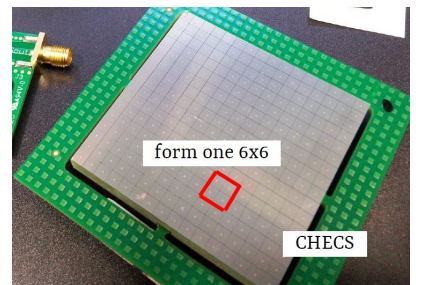
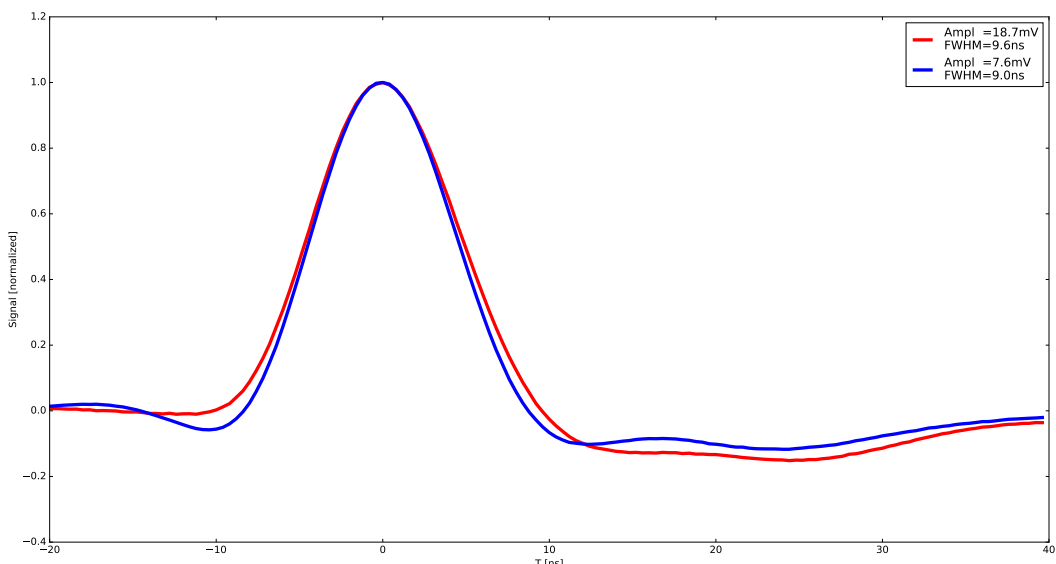


Figure 24: CHEC-S tile



720 **Figure 25:** The average pulse shape of the 1photoelectron in blue and the 2photoelectron pulse
721 in red of HPK S12642 at 25° C and 67.8V, which is around the proposed operating
722 point. Both pulses are averaged over »1000 events and normalized to illustrate pos-
sible differences in pulseshape resulting from the utilized shaping electronics. Both
723 pulses have a FWHM of around 10ns and are nearly free of ringing. The resulting av-
erage amplitude of the 1p.e. pulse is later used to calculate the Gain in [mV/p.e.]
instead of [V*IntWin] by cross-referencing the 1p.e. amplitude at multiple bias-
voltages.

720 My measurements of the CHEC-S tile concentrate on the array as an as-is device. This means
721 all results, influenced by external factors outside the actual Silicon Photomultipliers physics,
722 are valid on the assumption, that the way I was conducting the measurements is the way the

Photomultiplier will later be incorporated into the camera. On that ground, deviations of my results from the results of other groups and the manufacturer itself are expected. To clarify this further, I expect, for example, that the tests done at Hamamatsu Photonics where conducted on a single 3mm^2 pixel, not an array of 256 pixels, where 4 are tied together. Also divergence of shaping and amplification electronics between the groups will result in some differences. For this test, the CHEC-S tile is connected to the CHEC-S buffer, supplied with $\pm 4\text{V}$, where the signal is amplified. This signal in turn is then shaped via the CHEC-S shaper, developed by the University of Leicester. This is done in order to lower the unshaped pulse from a FWHM in the 100s ns to 10ns. This whole amplification and shaping chain is simulating later usage in the TARGET modules. I conducted the measurements multiple times on different pixels of the CHEC-S tile (appendix555657).

6.2.1 Gain

As described in section 3.1, the average pulse shape fig(25) is used to convert the relative gain from the analysis procedure to an absolute gain in sensible units. This is necessary, because the analysis aims to use pulse-area rather than -height, which results in this relative gain being in units of $V * \text{timebins}$, instead of plain V. In Figure (??) (left) the relative gain is shown, the right side shows the gain after conversion. A lower gain with increasing temperature is expected and described in detail in the chapter 3.1. In short, increased lattice movement due to higher temperature hinders photoelectron transport. The effects visible at extreme bias-voltages at both ends are partially analysis related. The gain of a SiPM is expected to be linear over bias-voltage at a constant temperature.

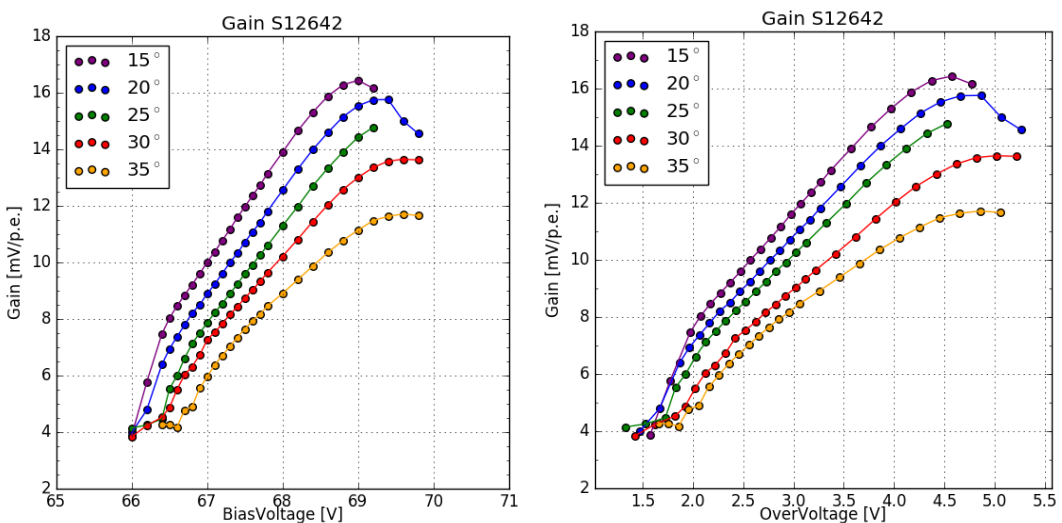


Figure 26: Gain of the HPK S12642 pixel, plotted against over-, bias-voltage and temperature.

In the lower regime at $V_b = 66.5\text{V}$ my analysis method struggles to pick up pulses, because of the very low gain compared to the noise. Depending on the chosen peak-finding threshold, I expect the analysis to interpret noise peaks as 1p.e. peaks at an increasing rate, the lower the

748 overvoltage is. This is visible in the sudden break in linearity at 30° C and 35° C , where the gain
 749 is almost in a plateau, due to this effect. The roll-over of the gain at the highest bias-voltages is
 750 in part a result of a voltage drop across the bias resistor occurring, because of high current flow
 751 through the SiPM. At higher temperatures, and therefore higher dark rates, the effect occurs
 752 at lower over-voltages. A second influence is caused again, by the noise at Vov 5V, which is
 753 very high compared to the proposed point of operation at Vov 3V. The same threshold is again
 754 counting the now increased noise peaks as 1p.e. peaks, but due to the abundance of 1p.e. pulses
 755 this just results in an apparent lowering of the gain.

756 6.2.2 Dark Count Rate

758 The Dark Count Rate is expected to increase with temperature, which is the case for S12642
 759 showb in Figure (27). I also expect it to follow a nearly linear progression, a sudden turn-up
 760 or turn-down of the Dark Count Rate would be analysis related. The turn-up at a certain point
 761 is visible in Figure (27), particulary for 15° C (purple) and 20° C (blue) respectively. At 15° C
 762 and an Overvoltage of 4V, the Dark Count Rate starts to deviate from the previously linear be-
 763 haviour. It starts to rise more rapid than before, which I can attribute to the fact, that the Optical
 764 Cross Talk at that point is very high; higher than 50% fig(28) (left). I suspect that I do not reach
 765 this critical point for the higher temperatures of 25° C (green) and 30° C (red), so the effect is
 barely, if not at all visible. At 35° C (yellow) I suspect my analysis is not able to count every

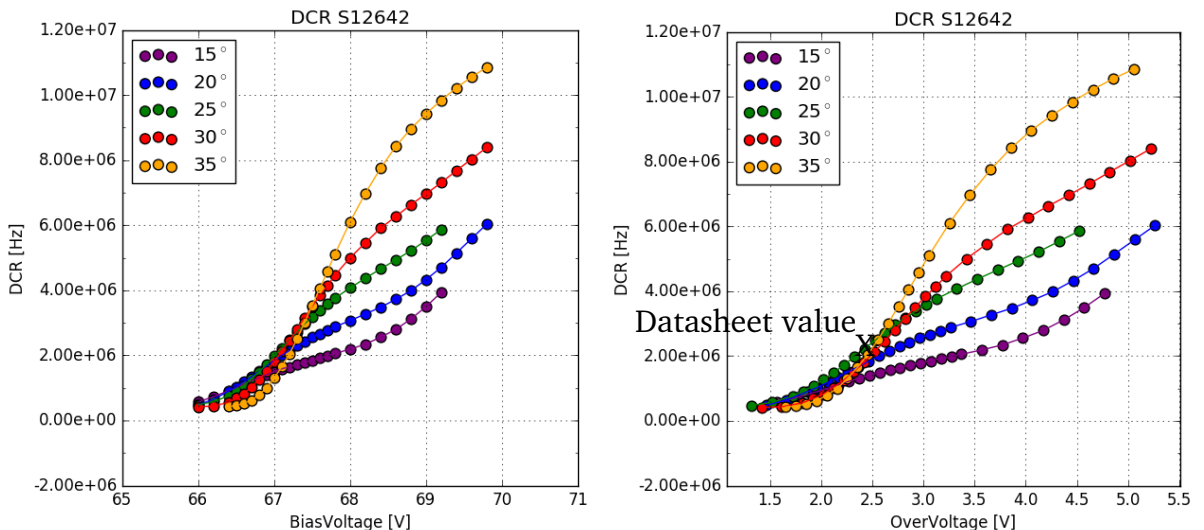


Figure 27: Dark Count Rate of the HPK S12642 pixel, plotted against over- , bias-voltage and temperature. Datasheet value at operation voltage = 2.4V and 25°C measured by current

766 pulse, due to the high rate of 9-10 MHz. A majority of the pulses overlapping each other and
 767 being counted as a 2p.e. event rather than 2 1p.e. events would reduce the Dark Count Rate sig-
 768 nificantly. At this point, heating of the Silicon Photomultipliers surface due to the high rate could
 769

770 also affect the Dark Count Rate through shifting of the temperature slightly upwards, away from
771 35° C . So that the Dark Count Rate declared at 35° C is in reality the rate at higher temperatures.

772

773 At the lower end of the bias-voltage range, I suspect, that a major part of the found 1p.e.
774 pulses are actually noise related. So the Dark Count Rate changing to a plateau is expected.
775 This is also due to the fact, that my measurements are done with a fixed bias-voltage range.
776 Due to the increase of the breakdown-voltage with rising temperature, part of the measured
777 bias-voltage range corresponding to a very low over-voltage, attributes to this effect. In order
778 to reliably measure beyond an overvoltage of 2.5V in the lower range, the noise would need to
779 be improved.

780 781 6.2.3 Optical Cross Talk

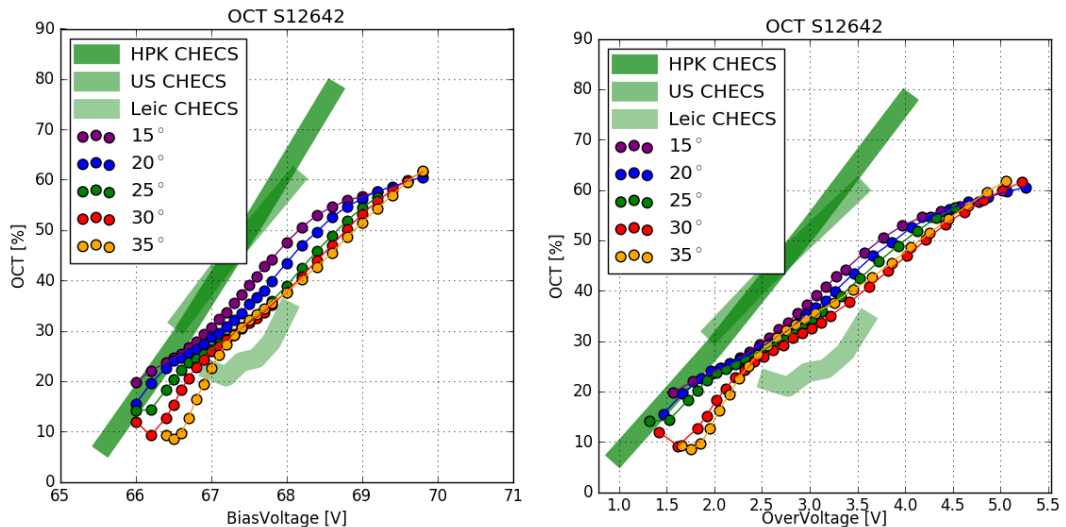


Figure 28: Dark Count Rate of the HPK S12642 pixel, plotted against over-, bias-voltage and temperature.

782 The Optical Cross Talk should be linear and independent from temperature. This is con-
783 firmed for HPK S12642. Minor deviations from that are probably due to slight errors in the
784 breakdown-voltage calculation from the gain regression line. The deviation of 30° C and 35° C
785 below an over-voltage of 2V stems from the way the gain regression line is used to calculate
786 both Dark Count Rate and Optical Cross Talk. At higher temperatures the lower voltage range
787 is dominated by noise, so using the gain regression line to calculate the Optical Cross Talk at
788 those low voltages leads to the visible effect of the first few datapoints of 30° C and 35° C. The
789 deviations between the different groups results at 25° C (green) are caused by 4 major con-
790 tributions. Firstly the difference in the tested device. While I take measurements on 4 3mm²
791 pixels electrically tied together, the way the device will later be implemented into CHEC-S, the
792 groups in the US and Hamamatsu Photonics are likely to run tests on 1 3mm² pixel only. Sec-
793 ondly I suspect a slight difference in amplification and shaping electronics. The measurements

794 I conducted as well as the measurements of Leicester are done with the same shaper and buffer
795 configuration. The difference here is, thirdly, my measurements are done with dark counts only,
796 while measurements from other groups are conducted with a pulsed light source and reading
797 out timed windows. This causes the results from Leicester to be difficult to compare against,
798 their surface temperature of the SiPM is likely much higher than 25° C, and thus, a misinter-
799 preted breakdown-voltage at 25° C causes a shift of the Optical Cross Talk to the right. Lastly
800 the difference in actual data taking and analysis procedure must be mentioned, also this is only
801 of minor concern, as we will see with other measured devices.

802 6.3 Hamamatsu LCT5 50 μ m 6mm

804 The Silicon Photomultiplier designated HPK S13360
805 6050CS fig(29) is an LCT5, meaning Low Cross Talk
806 5th iteration device from Hamamatsu Photonics. It is
807 one of the most promising candidates for later usage in
808 CHEC-S. It has a pixelsize of 6mm² consisting of 14400
809 cells with a cellsize of 50 μ m. The present device and
810 its similar iterations are the first to incorporate trenches
811 bordering each cell, effectively insulating the cells and
812 reducing the prompt Optical Cross Talk very effectively.
813 Tests are done with a single pixel only, in contrast to
814 measurements done on S12642. It is mounted on a
815 ceramic chip and coated with a silicon resin that is UV-
816 transparent. Wire bonds supply the electrical contact. A similar, but not tested, device from
817 the same generation uses through-silicon-via (TSV) technology, realising electrical connection
818 through the silicon bulk, allowing a tighter fit of the cells, with minimal dead-space.

LCT5 6mm

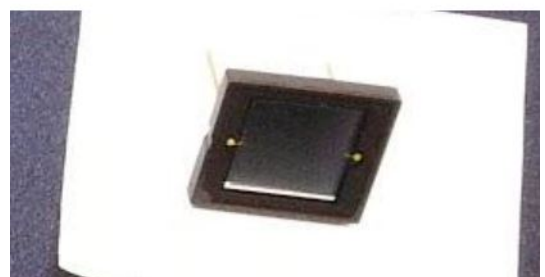


Figure 29: HPK S13360 6050CS pixel

A similar, but not tested, device from the same generation uses through-silicon-via (TSV) technology, realising electrical connection through the silicon bulk, allowing a tighter fit of the cells, with minimal dead-space.

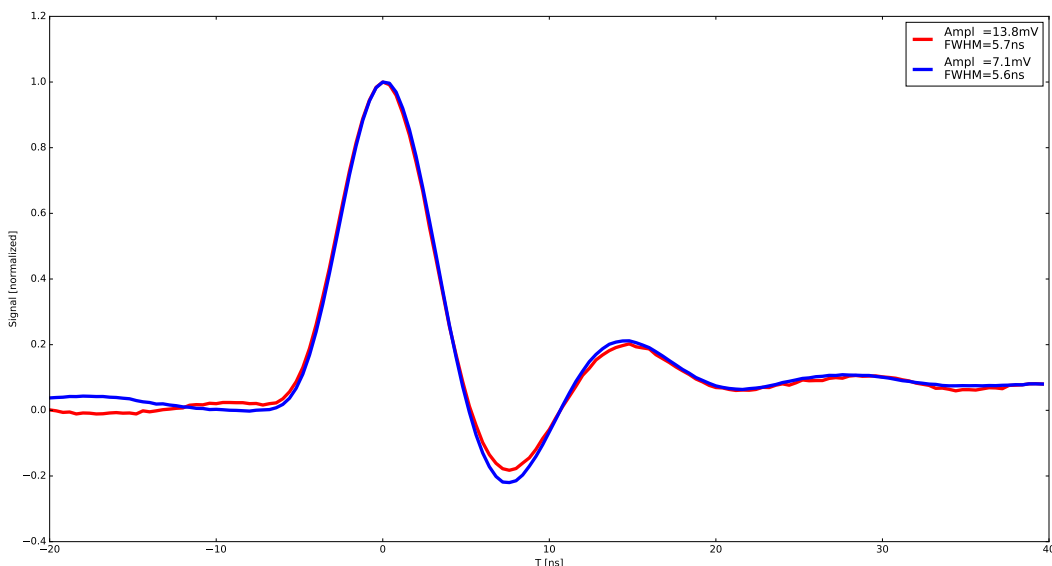


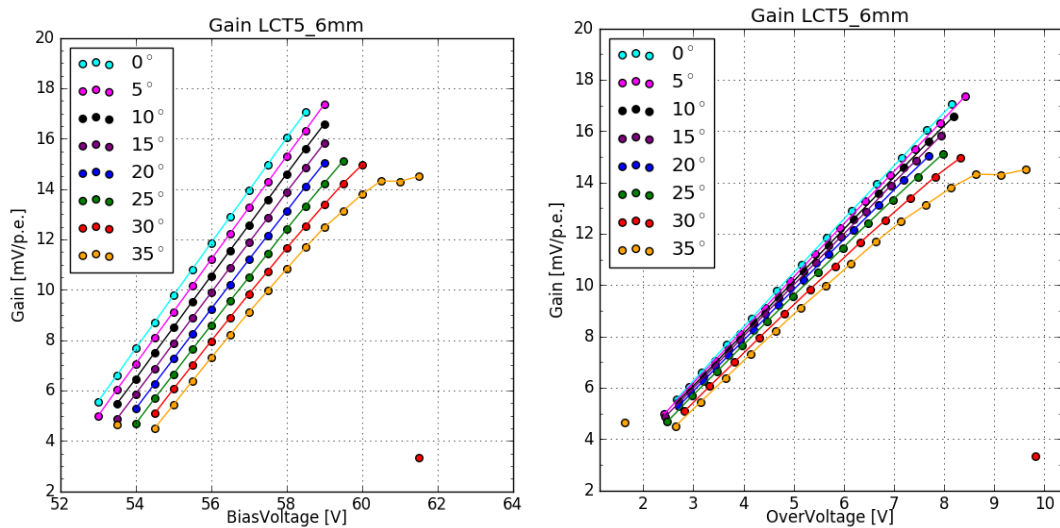
Figure 30: The average pulse shape of the 1photoelectron in blue and the 2photoelectron pulse in red of HPK S13360 6050CS at 25° C and at point of operation. Both pulses have a FWHM of around 5ns and ring for approximately 20ns with an undershoot of 20%.

819 The layout of the single pixle test device made external amplification necessary. I used a
820 MiniCircuits PreAMP, which was supplied with 13V during this test. Shaping of the pulse is
821 conducted by a CHEC-S shaper, modified to fit the new unshaped pulse. The pulse shape fig(30)
822 makes the pulses appear much harder to analyze, due to the possibility of events occurring during

823 the ringing window. This assumption proved untrue, due to the devices low Dark Count Rate
824 and Optical Cross Talk, so the multi incident probability is also low.

825 6.3.1 Gain

827 The gain of the LCT5 50 μ m 6mm device is clearly linear with some minor outliers at 30°C.
828 The same effect as with S12642 is visible at 35°C, again counting noise peaks as 1p.e. peaks,
829 resulting in an apparent lowering of the gain and the slope changing over into a plateau. In
830 Figure(31)(left) the gain is shown, plotted against over-voltage. It is still dependant on tem-
831 perature, but due to reliable breakdown-voltage calculation, the spread is much smaller than,
832 if plotted against bias-voltage. The same conversion is done to transform relative gain into an
833 absolute gain with sensible units. When parametrized with over-voltage, the gain is essentially
temperature independent.



834 **Figure 31:** Gain of the HPK S13360 pixel, plotted against over-, bias-voltage and temperature.

835

836 6.3.2 Dark Count Rate

837 The Dark Count Rate of two similar HPK S13360 devices is shown in Figure(32). The bars
838 show the difference between the two devices, the results of one device is used as a reference,
839 while the deviation is illustrated with the filled bar. The Dark Count Rate of HPK S13360
840 follows the expected behaviour, mostly linear in the significant range and rising with increasing
841 temperature. Below an over-voltage of 2.5V my analysis struggles, I suspect the gain, compared
842 to noise, to be too low for my analysis to pick up pulses. Thus the regression line calculation is
843 unreliable in this range. The turnup at high over-voltages is most prominent at 0°C(teal) after
844 an over-voltage of 9V. This is also the point where the Optical Cross Talk rises very rapidly.

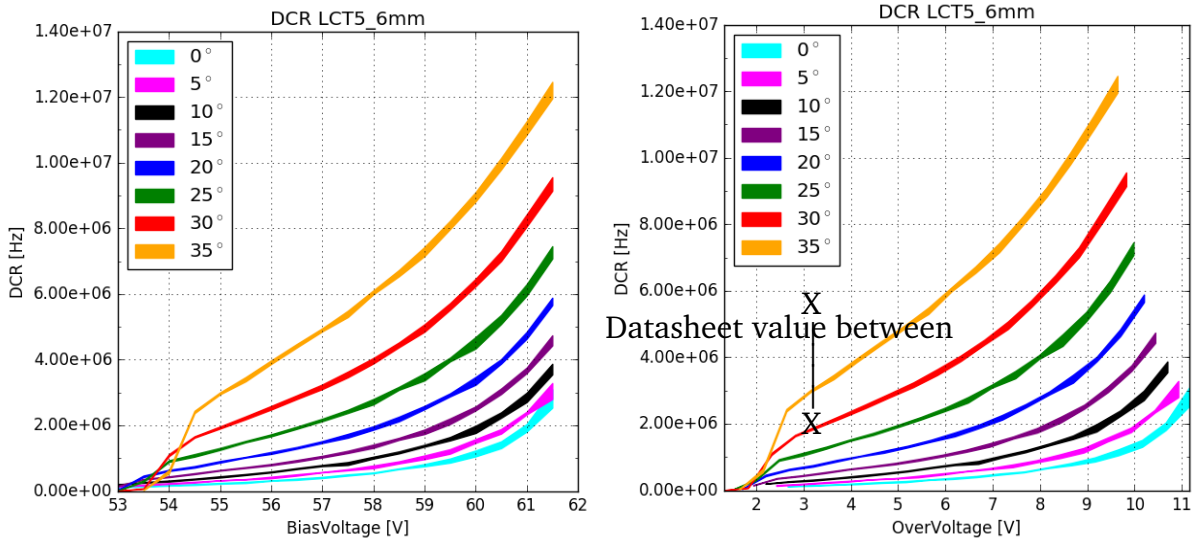


Figure 32: Dark Count Rate of the HPK S13360 pixel, plotted against over-, bias-voltage and temperature. The Datasheet value at 25°C of the DCR at $V_{OV} = 3V$ covers a very large range to exactly compare against, and is measured by current

845 6.3.3 Optical Cross Talk

846

847 Compared to measurements on HPK S13360 done at the Nagoya University, Japan fig(33)
 848 (faded green bar), I see a very strong correlation of the Optical Cross Talk in the over-voltage
 849 range between 2.5V and 9V. The Optical Cross Talk in this range is linear and independent from
 850 temperature, with minor deviations attributed to the breakdown-voltage calculation from the
 851 regression line, causing the horizontal shift. In contrast to my technique, using only dark counts,
 852 the measurements at Nagoya University followed a pulsed light source approach, reading out
 853 a time-window after the laser incident. This could have consequences, since Optical Cross talk
 854 with a large delay time could be missed. Deviations below an over-voltage of 2.5V are expected,
 855 they are very likely caused by the regression line calculation being unreliable in this range due
 856 to the analysis method struggling to pick up pulses using dark counts. Above an over-voltage
 857 of 9V, which is also the point of the turnup of the Dark Count Rate, the Optical Cross Talk is
 858 no longer linear and the deviation from the results of Nagoya University increase very rapidly.
 859 I suspect the rapid increase in both Dark Count Rate and Optical Cross Talk to be caused by
 860 the over-voltage reaching ranges, where interpretation of noise as a 1p.e. pulse becomes more
 861 likely. This, joint together with the usage of the MiniCircuits amplifier supplied with 13V, makes
 862 false interpretation of noise as pulses even more likely. I suspect these two reasons in conjunc-
 863 tion are responsible for both, the sudden rise of the Dark Count Rate as well as the deviation of
 864 the Optical Cross Talk from linearity and the results of Nagoya University, above over-voltages
 865 around 9V. In summary, the correlation between the two measurements, conducted by two dif-
 866 ferent methods of data acquisition and analysis, is evident.

867

868

869 The S13360 series is the first to incorporate physical barriers, called trenches, effectively insu-
 870 lating the cells from each other. This drastically reduces the prompt cross-talk, while increasing
 871 the percentage the delayed cross-talk contributes to the overall cross-talk shown. This could
 872 also be the reason for the upturn compared to data from the University of Nagoya, at higher
 873 over-voltages the contribution from delayed cross-talk is higher. With the trenches effectively
 874 reducing the prompt cross-talk and the difference in analysis, the effect could be partially ex-
 875 planed by increased contribution of the delayed cross-talk. More on this subject in chapter
 876 7.

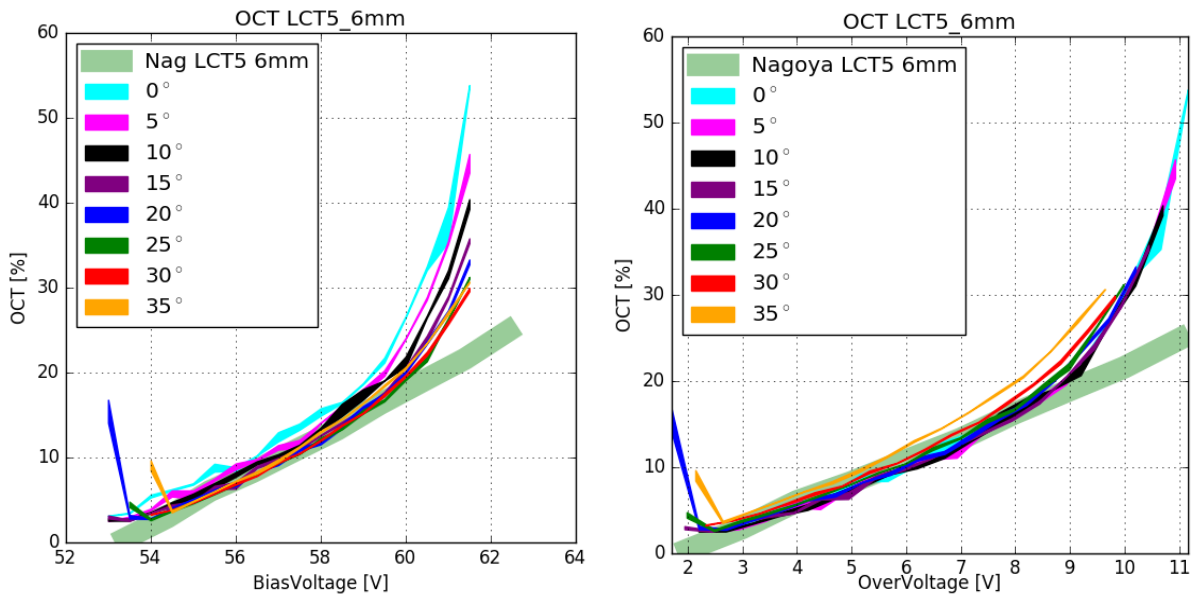


Figure 33: Optical Cross Talk of the HPK S13360 pixel, plotted against over-, bias-voltage and temperature.

877 6.4 Hamamatsu LCT5 75 μ m 7mm

879 XXXXXXXXXX is a larger LCT5 prototype Silicon Photo-
880 tomultiplier of the same design as S13360-6050CS
881 fig(34). With an increase in cellsize to 75 μ m, the de-
882 vice gains a higher fill-factor than 50 μ m devices. The
883 pixel-area is also expanded to 6.915mm², which will re-
884 sult in a higher fill-factor (less deadspace), so presum-
885 ably a higher PDE but also a higher OCT. Since it is a
886 prototype device, there is limited data from datasheets.
887 The ID number suggests, that it is also a wire-bond de-
888 vice with a UV-transparent silicon-resin coating. It is
889 also a single pixel test device, so external amplifica-
890 tion is necessary with the MiniCircuits PreAMP, sup-
891 plied with 8V during this test. The signal is also shaped by a differently modified CHEC-S
892 shaper, which results in a pulse shape similar to S12642, but with a much lower amplitude
893 fig(35).

LCT5 7mm



Figure 34: HPK LCT5 7mm pixel

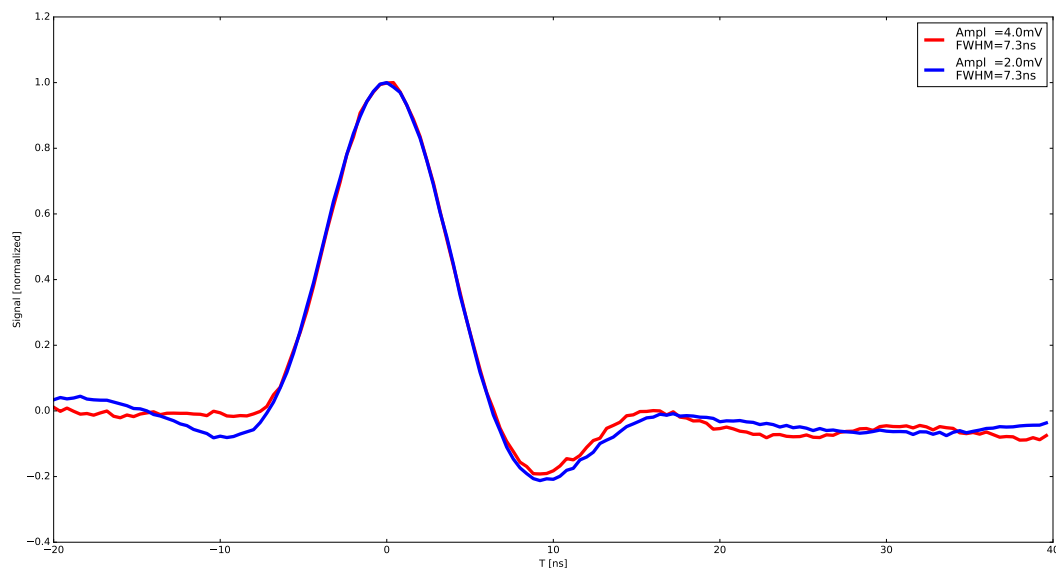


Figure 35: The average pulse shape of the 1 photoelectron in blue and the 2 photoelectron pulse in red of HPK LCT5 7mm at 25° C and at point of operation. Both pulses have a FWHM of around 7ns and an undershoot of 20%, with no ringing.

894 6.4.1 Gain

896 Figure(36) shows the gain of the LCT5 7mm de-
897 vice. Two sets of measurements are done for 25°C
898 to extend the measured range. The first set of mea-
899 surements covers the lower over-voltage range,
900 where the low gain makes external amplification
901 necessary with a MiniCircuits PreAMP supplied
902 with 8V. I chose the lowest possible amplification
903 of the PreAMP, so that reaching the point of sat-
904 uration of the oscilloscope input is as late as pos-
905 sible as the over-voltage rises. Saturation of the
906 oscilloscope occurs due to the possibility of gen-
907 erating very large p.e. (>10 p.e.) events at the
908 higher over-voltages, which are saturating the in-
909 put. Joint together, the LCT5 7mm device and the
910 MiniCircuits PreAMP at 8V reach this point at an
911 over-voltage of ~ 6 V. In Figure(36) the results from

912 the lower range measurement are displayed as the lower-range green line extending between an
913 over-voltage of 1.6V to 5.4V. The configuration for the second test removes the PreAMP from the
914 setup, which makes the lower over-voltage range unaccesible, but extends the range to higher
915 over-voltages. This configuration reaches the point of saturation at an over-voltage of ~ 8 V. The
916 higher range measurement results are displayed as the second green line (25°C) extending from
917 3.4V to 7.2V over-voltage in Figure(36). There is a clearly visible overlap of the two measure-
918 ments between ~ 3.4 V and ~ 5.4 V . It also seems, that the gain dependency on temperature is
919 reversed. While for all other devices, the gain lowers with rising temperatures, the LCT5 7mm
920 device seems to show inversed behaviour. This inverse behaviour is caused by the calculation of
921 the breakdown-voltage from the gain-regression line, with this and the bias-voltage, the over-
922 voltage is calculated, causing a horizontal shift. Plotting the gain versus bias-voltage, however,
923 shows the expected behaviour.

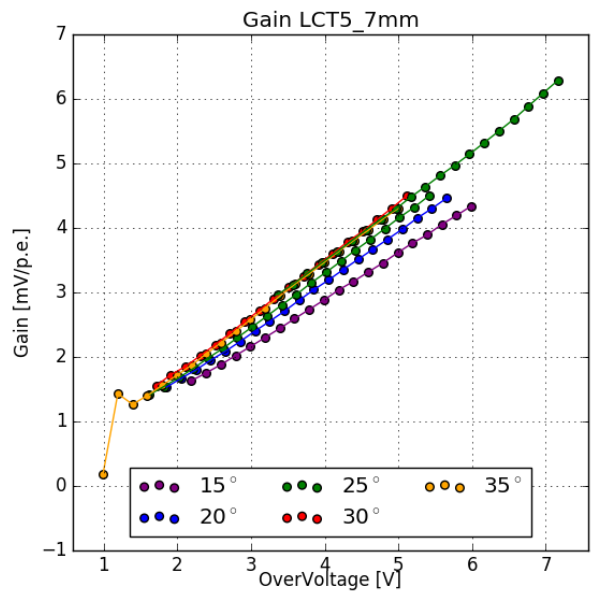
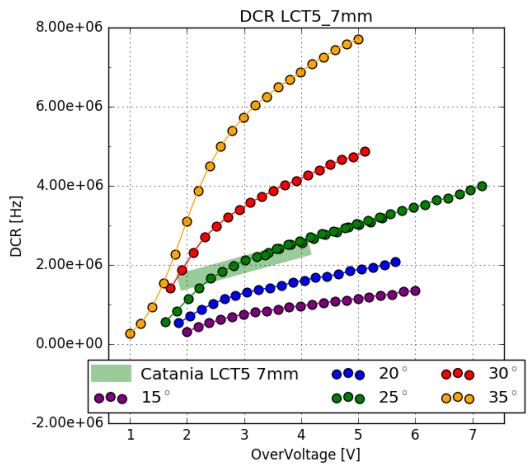


Figure 36: Gain of the HPK LCT5 7mm pixel

924 6.4.2 Dark Count Rate

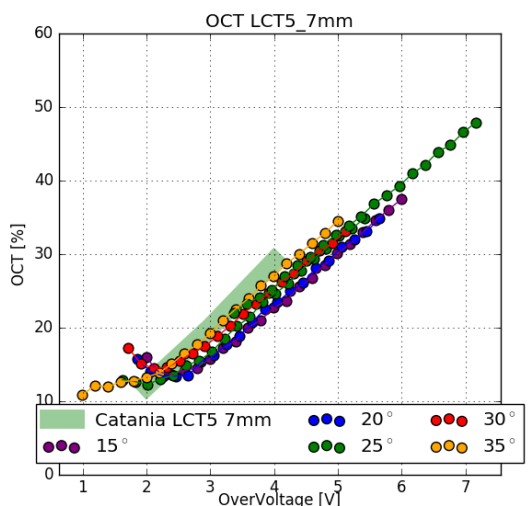
926 The behaviour of the Dark Count Rate of the HPK LCT5
927 7mm device is shown in Figure(37) and is as expected,
928 in contrast to the behaviour of the gain of LCT5 7mm,
929 as discussed in section 6.4.1. It follows a linear pro-
930 gression in the relevant range and increases with rising
931 temperature. I suspect the over-voltage range above
932 $\sim 2.5V$ to be relevant. The extended range measure-
933 ment at $25^{\circ}C$ confirms this behaviour. LCT5 7mm
934 shows a linear Dark Count Rate over an over-voltage
935 range of 4V. The faded green bar in Figure(37) shows
936 results from measurements undertaken by the Depart-
937 ment of Physics and Astronomy at the University of
938 Catania. Those measurements were conducted on the
939 exact same device, which is an important point, but
940 with a different method of data acquisition and data analysis. Analysis techniques are discussed
941 in chapter 7. The correlation between the two experiments is evident, although there is differ-
942 ences in the acquisition and analysis process. This is further proof for the relevancy of the
943 analysis technique employed in this paper.



944 **Figure 37:** Dark Count Rate of the HPK
945 LCT5 7mm pixel

6.4.3 Optical Cross Talk

946 The Optical Cross Talk is expected to be linear and in-
947 dependent from temperature. This is the case in the, in
948 section 6.4.2 established, relevant over-voltage range
949 of above $\sim 2.5V$. Minor deviations are attributed to the
950 calculation of the breakdown-voltage from the gain-
951 regression line. The over-voltage is calculated from
952 the former and the supplied bias-voltage, which in turn
953 causes a slight horizontal shift. With that, comparing
954 my results to the measurements from the University of
955 Catania shows a strong correlation. Keeping in mind,
956 that the process of data acquisition and analysis is dif-
957 ferent for both measurements further proofs the analy-
958 sis technique valid.



944 **Figure 38:** Dark Count Rate of the HPK
945 LCT5 7mm pixel

959 6.5 Hamamatsu LVR 50 μ m 6mm

961 The Silicon Photomultiplier by Hamamatsu Photonics
962 with the designation 6050HWB-LVR-LCT is a special
963 prototype of the LCT5 design. LVR is an abbreviation
964 of Low Voltage Range, meaning the device is meant
965 to be operated at much lower operation voltages than
966 other LCT5 devices. It has the same physical size as an
967 LCT5 50 μ m 6mm device (S13360 chapter ??), a pix-
968 ellsized of 6mm pixel with a cellsize of 50 μ m. The rec-
969 ommended point of operation however is \sim 15V below
970 that of the S13360 device, specifically at 40.2V(LVR)
971 instead of 54.7V (S13360). The unshaped signal is
972 similar to other LCT5 devices, therefore using the same modified CHEC-S shaper is feasible
973 in this case, resulting in a similar pulse shape fig(40). After that the signal is amplified with the
974 same MiniCircuits PreAMP supplied with 8.5V.

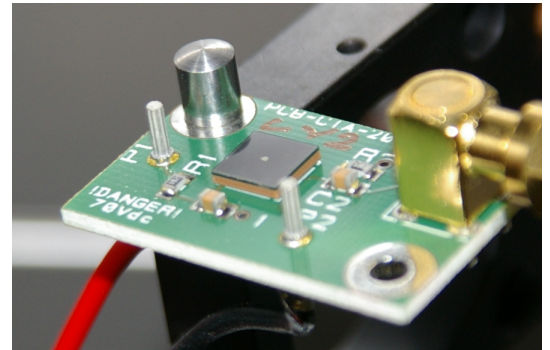


Figure 39: HPK LVR 6mm pixel

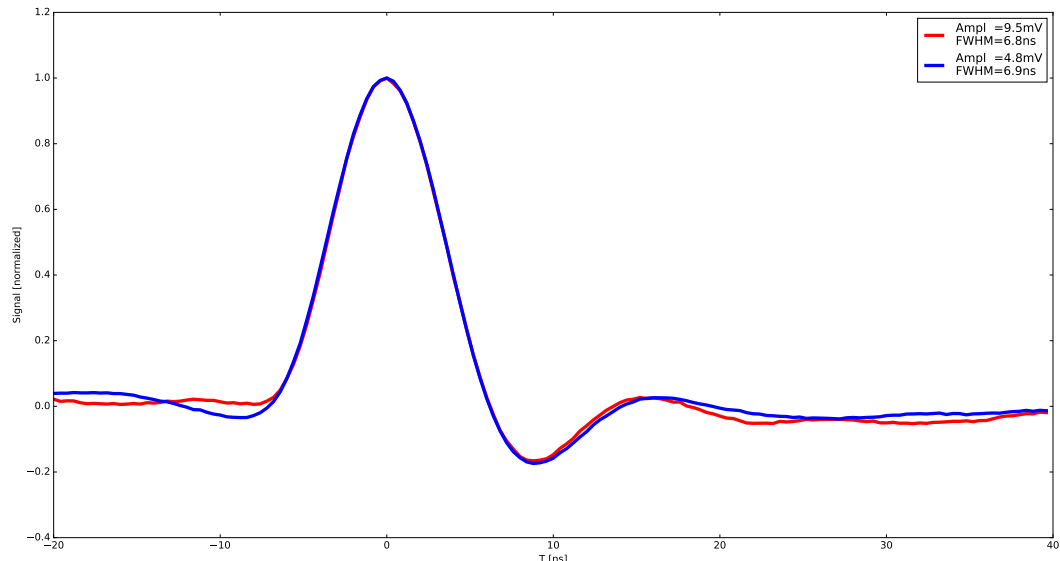


Figure 40: The average pulse shape of the 1photoelectron in blue and the 2photoelectron pulse in red of HPK LVR 6mm at 25° C and at point of operation. Both pulses have a FWHM of around 7ns and an undershoot of 20%, with no ringing.

976 6.5.1 Gain

978 Figure(41)(right) shows the gain of the LVR 6mm device. It is, as expected, linear over a
979 long range and nearly independent of temperature when parametrized with over-voltage. The
980 flattening of the slope to a plateau shape in the lower over-voltage range, is caused by the

analysis being unable to identify peaks lower than the set threshold. Only taking into account the linear region, limits the range, where the results are relevant to an over-voltage range of ~ 2.5 V. Saturation of the oscilloscope in this range is not visible, but a check with a more expanded range revealed, that the point of saturation of the oscilloscope is at an over-voltage of ~ 5 V. The apparent overlap of the gain, when plotted against over-voltage, is based on the calculation of the breakdown-voltage being very reliable due to the large linear range. Plotted versus bias-voltage fig(41)(left) the expected behaviour of the gain, lowering with increasing temperature, is visible.

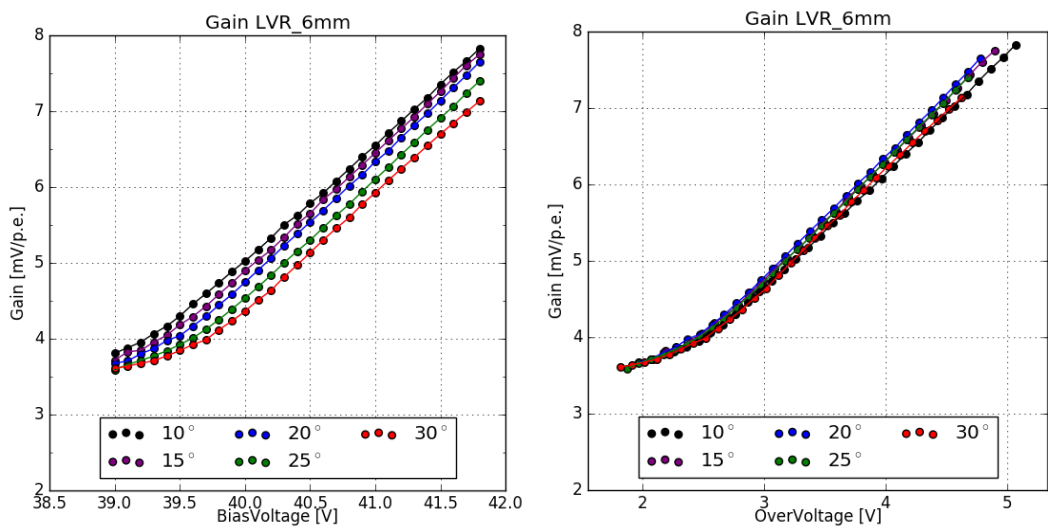


Figure 41: Gain of the HPK LVR 6mm pixel

988

989 6.5.2 Dark Count Rate and Optical Cross Talk

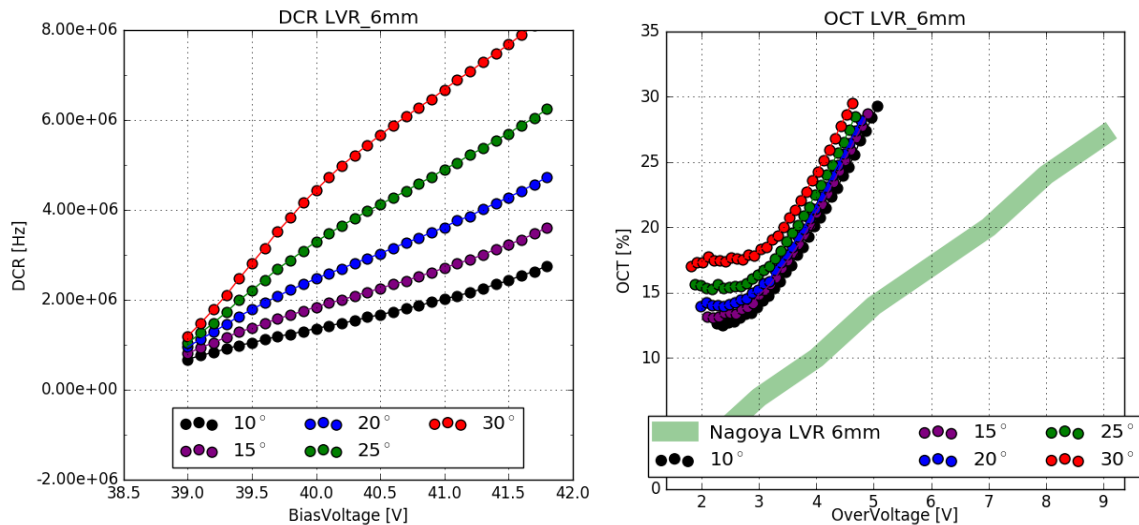


Figure 42: Dark Count Rate and Optical Cross Talk of the HPK LVR 6mm pixel

991 The Dark Count Rate fig(42)(left), taking into account only the relevant over-voltage range
992 of $>\sim 2.5V$ seems to correlate, while the resulting Optical Cross Talk fig(42)(right) is very high
993 compared to results from the University of Nagoya, which also cover a much wider range.
994 Only taking into account the previously established relevant over-voltage range of $>\sim 2.5V$, the
995 resulting Optical Cross Talk is a factor of 2 higher. This uncertainty is a contrast to results
996 from previous devices, where strong correlations between different groups and measurement
997 techniques are evident. I suspect, that the device examined by me and the device present at
998 Nagoya University are slightly different prototypes.

6.6 SensL FJ60035 6mm 35 μ m

The Silicon Photomultiplier by SensL with the designation FJ-60035 is also a candidate device for use in CHEC-S. It is also a 6mm device, but with a much smaller cellsize of 35 μ m, using the TSV technology, so there are no wire-bonds present. This results in 22292 cells on a single pixel with a fill-factor of 75% . It is coated with plain glass. The recommended point of operation is around 30V bias-voltage, lower even than that of the HPK IVR prototypes. The device is, by the manufacturer, pre-mounted on a printed circuit board, called a test array. This test array contains a fast output, that directly couples to the cells, and a slow output, conventionally read out via the quench resistor. For the conducted tests, I used the fast output amplified with the MiniCircuits PreAMP supplied with 12V. The SensL device was the first device measured, therefore the analysis procedure used was an older iteration compared to the procedure for the Hamamatsu devices.

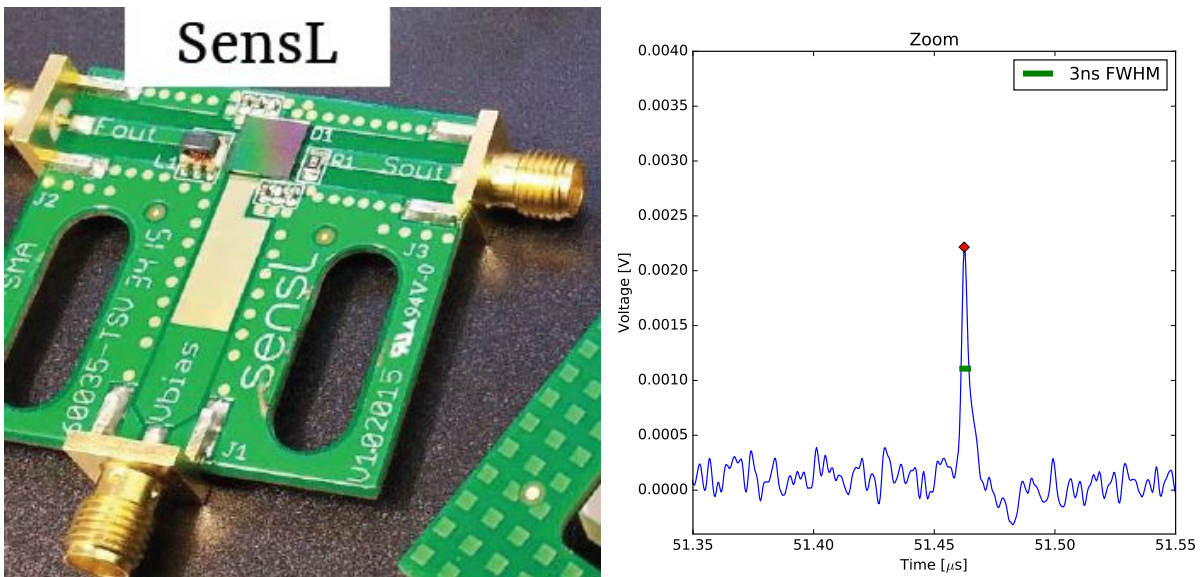


Figure 43: SensL Test Array and pulse shape at $V_{bias-voltage} = 29V$

6.6.1 Gain

Evaluating the SensL pulse area spectra shows the 1 p.e. position and Δ p.e. overlapping, so using the older analysis iteration introduced no error when evaluating the gain of the SensL device. It is clearly linear over a wide temperature range from -5°C to 35°C over an over-voltage ranging from 2V up to 8V. When plotted versus over-voltage the spread of the gain is even tighter signaling slight temperature independency, but still following the expected behaviour of decreasing with increasing temperature.

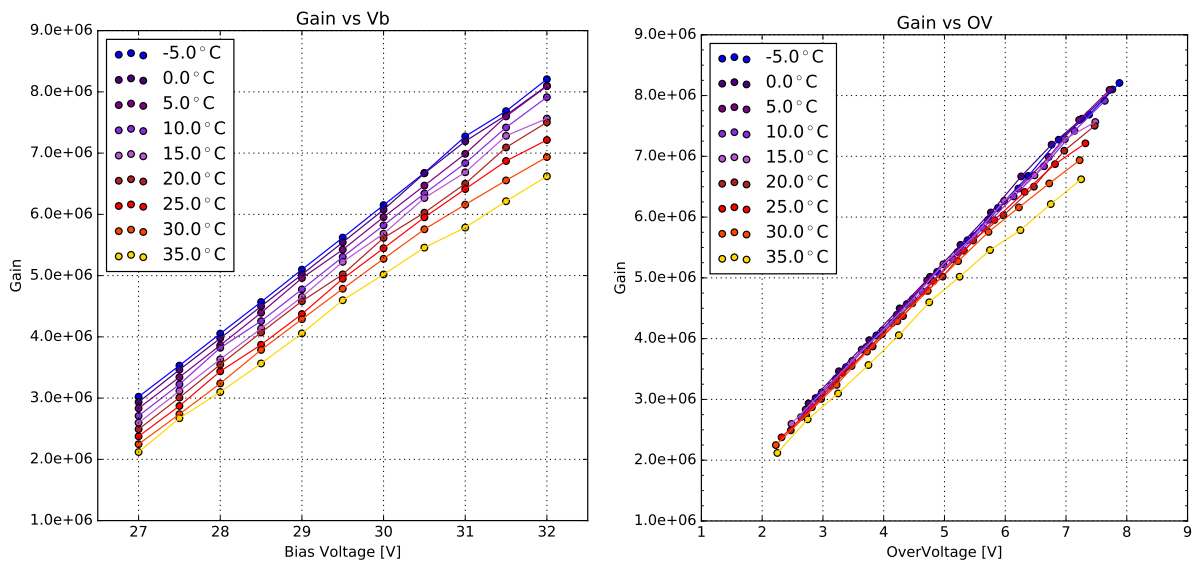


Figure 44: Gain of the SensL FJ-60035 test array

6.6.2 Dark Count Rate and Optical Cross Talk

The Dark Count Rate fig(45)(left) also shows the expected behaviour. At very low temperatures the changes in rate over the over-voltage range is minimal. Increasing the temperature shows a rapid increase in thermally induced dark counts. The Optical Cross Talk fig(45)(right) on the other hand is independent of the device temperature, also as expected.

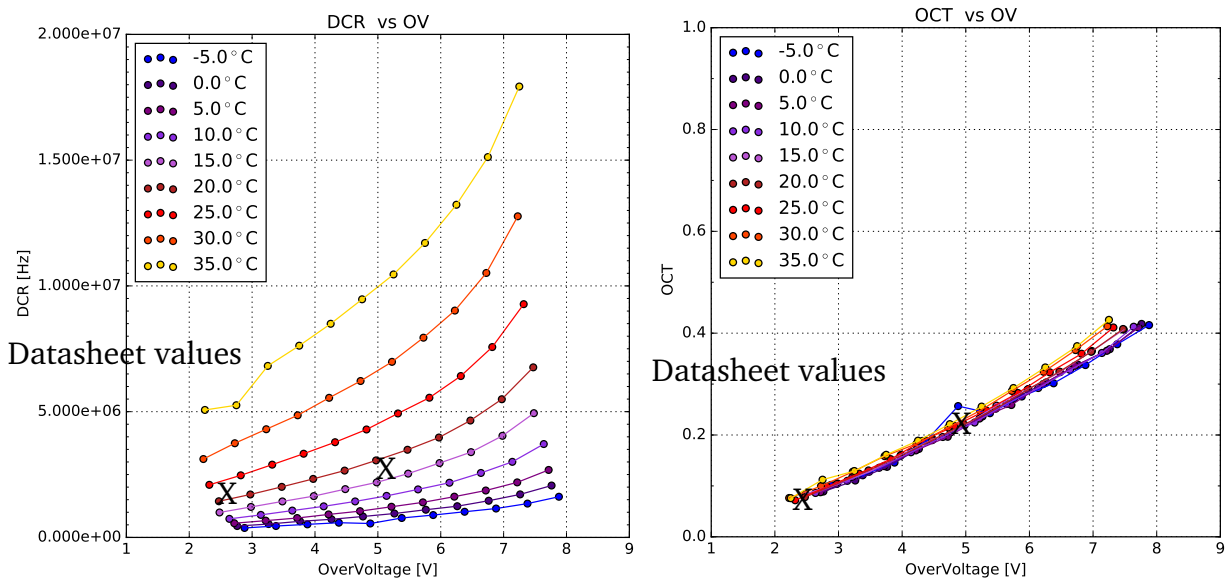


Figure 45: Dark Count Rate and Optical Cross Talk of the SensL FJ-60035 test array. Datasheet values measured at 21°C(~dark red). Adding nagoya results later

1026 7 Comparison

1028 A comparison of the performance of all devices is the significant step for choosing the Silicon
1029 Photomultiplier later to be used in CHEC-S. In order to do this, all measured characteristics are
1030 compared versus over-voltage. Operation of the CHEC-S camera in GCT will come down to a
1031 decision between two operational points. The first point will be marked by an Optical Cross Talk
1032 of under 15%. Every other attribute of the Silicon Photomultiplier at this over-voltage is then
1033 compared. This point will trade off precision for efficiency, a lower Optical Cross Talk makes
1034 real event detection easier, on the other hand, a lower Photon Detection Efficiency may forfeit a
1035 lot of potential data.

1036 The second point of operation is marked at the highest achievable Photon Detection Efficiency.
1037 My conducted measurements do not involve this, other groups are comissioned to determine
1038 the point of highest Photon Detection Efficiency, in other conducted measurements, that are
1039 comparable 48. This point will assure the highest detection of event photons, but will trade
1040 that for an increase in detector noise, due to the higher Dark Count Rate and more importantly
1041 Optical Cross Talk.

1042 Comparing results to other groups is shown in Figure (46), using different experimental setups
1043 and procedures and therefore also entirely different analysis techniques. Comparing against
1044 results from the University of Leicester, the University of Nagoya and the University of Catania,
1045 all of which are conducting fixed window readout of the SiPM after an expected light-pulse from
1046 a flasher-LED or pulsed laser.

1047 7.1 Dark Count Rate

1049 Comparing the Dark Count Rate of the measured devices and results from the other groups is
1050 shown in Figure 46. The differences in analysis procedure will only have a slight impact on the
1051 presumed Dark Count Rate, since all experiments record dark-count events over their respective
1052 acquisition time windows. On the other hand, if the readout window is sufficiently small, events
1053 originating from afterpulsing or delayed crosstalk could be missed. All groups experience the
1054 same multi-hit coincidence, meaning a light-event or dark-event coinciding with another, forming
1055 a (partial)multi p.e. event.

1056 Only two of the 5 measured device have measurements results from other groups to compare,
1057 as it is not their focus. In the case of both, the LVR 6mm and the LCT5 7mm results can be
1058 discussed to some degree as matching. While the correlation is obvious for the LCT5 7mm de-
1059 vice Figure(??)(red), where the covered measurement range in this paper exceeds the external
1060 results, while matching and showing the same trend, the LVR 6mm results deviate. Between an
1061 over-voltage of 3V and 4V the results overlap, the trend on the other hand is obviously different.
1062 Additionally the limit on the higher range due to noise makes it impossible to compare against

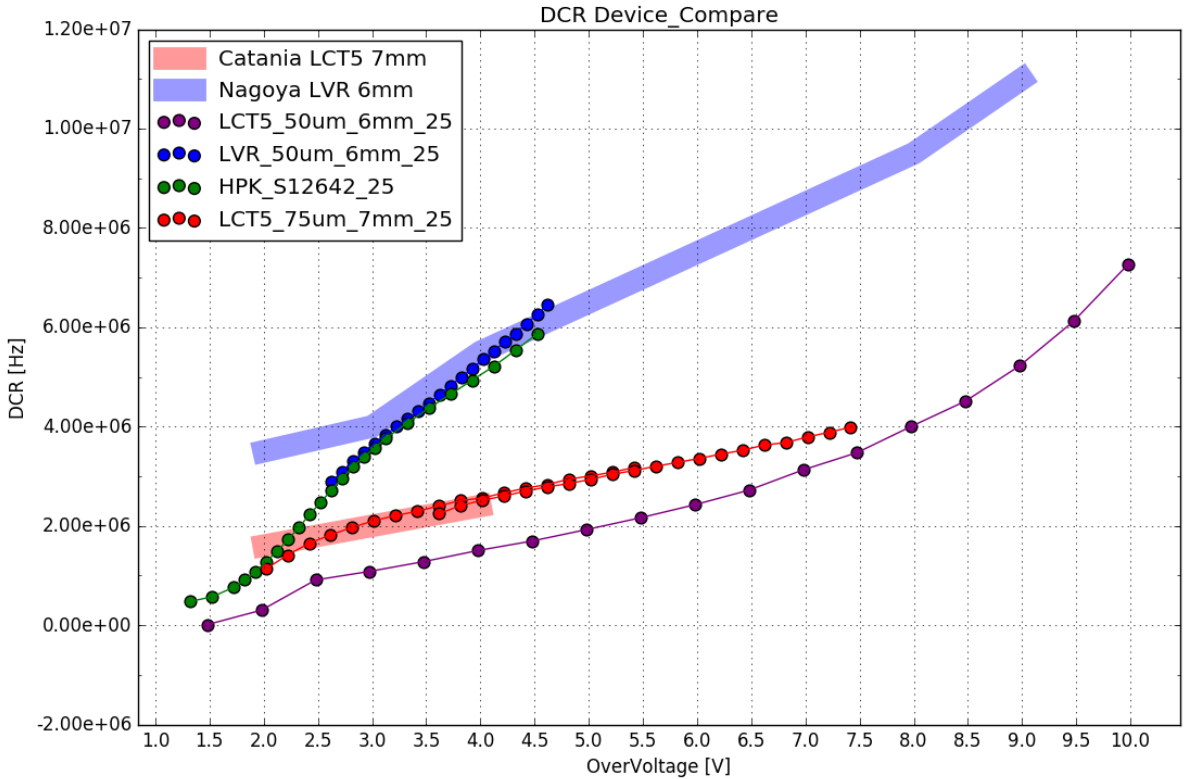


Figure 46: Dark Count Rate comparison of measured devices at 25°C. Description

1063 the full range measured by the external group, so the DCR for LVR 6mm must be labeled as not
 1064 matching.

1065 7.2 Optical Cross Talk

1066
 1067 The comparison of the Optical Cross Talk between the different groups and the results presented
 1068 in this paper are dependant of the analysis and acquisition procedure. Extended trace analysis,
 1069 utilized in this paper captures all aspects of the Optical Cross Talk, prompt and delayed as well
 1070 as afterpulsing. The procedure of time window analysis, utilized by the groups being compared
 1071 to, are, due to their limited window, either biased towards the prompt cross talk or in extreme
 1072 cases, will not be able to capture delayed cross talk or time-delayed afterpulsing at all. Com-
 1073 paring data analysis techniques, for example, at the University of Leicester is therefore a vital
 1074 step. Their approach utilizes a pulsed laser as light source and involves no cooling of the SiPM
 1075 tile. The waveforms are extracted from the scope and a small time window is defined from
 1076 the known time position window of the incident pulse to search for peaks, find their value and
 1077 generate a histogram. To the pulse area histogram, a theoretical model of contributing factors
 1078 is fitted. This theoretical model simulates characteristics, updating continuously to find their cor-
 1079 rect values. Those values are the full set of characteristics of the device in testing, among them:
 1080 gain curve, breakdown-voltage, OCT, PDE, noise, dynamic range, crosstalk probability.
 1081 There are a number of differences in their approach compared to the one utilized in this paper,

most important is the time window size. If the window after an incident pulse is too short, data loss is a possibility, depending on the delay time of delayed cross-talk and afterpulsing assisted by traps with long lifetimes. This is a problem, especially with devices of the LCT5 generation implementing physical trenches isolating the cells and effectively reducing the prompt cross-talk, the contribution from the prompt cross-talk to the overall Optical Cross Talk is lowered. For time window analysis with short window times, missing data from delayed cross-talk and afterpulsing, because it will not be recorded yet, would lead to errors in the overall Optical Cross Talk results being lower than expected.

1090

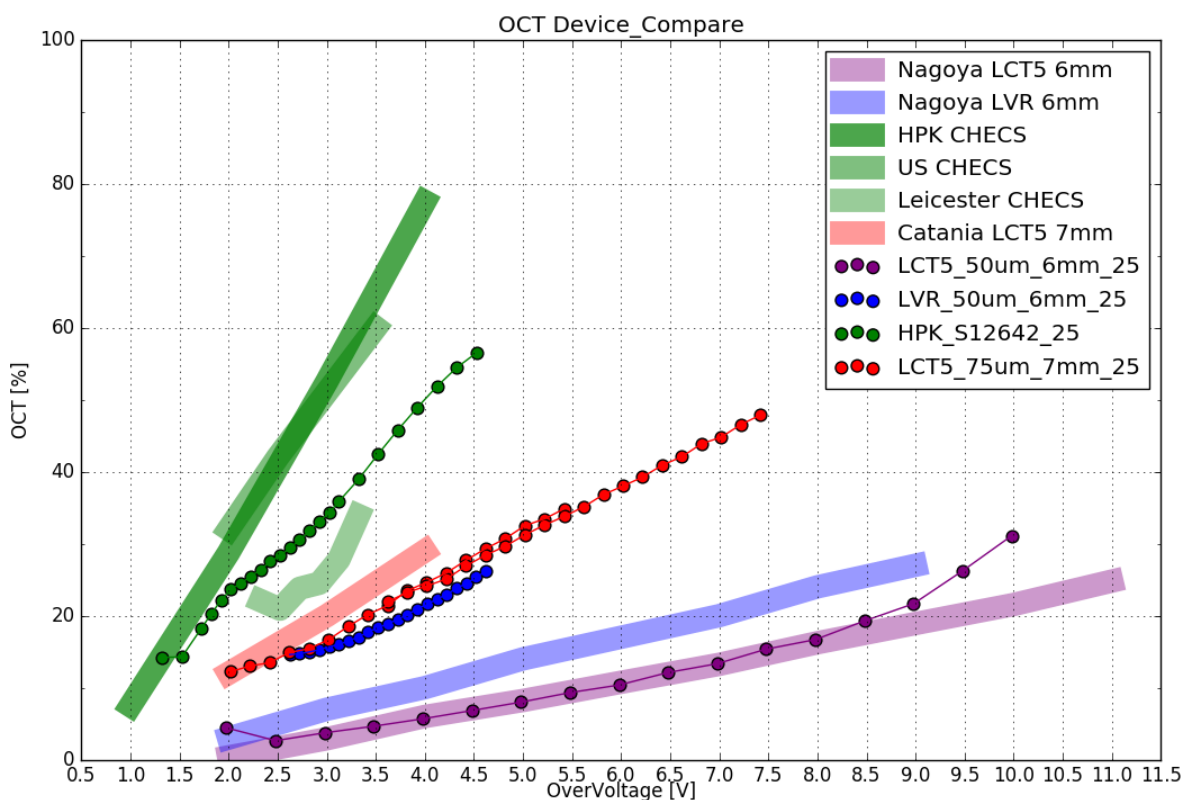


Figure 47: Cross Talk comparison of measured devices at 25°C. Description

This is indeed the case for the S12642 tile in Figure 47 (green). The light green bar below the dotted data presented in this paper shows the results form the University of Leicester indeed being lower. In purple results of the LCT5 S13360 device with physical trenches are shown. Compared to results from the University of Nagoya, there is a prominent upturn at around an over-voltage of $\sim 8V$. This could be due to the differences in analysis technique. The University of Nagoya also employs time window analysis. LCT5 posseses lowered prompt cross-talk probability, so the contribution of delayed cross-talk to the overall cross-talk is higher than for S12642. With rising over-voltage the ratio between prompt and delayed cross talk shifts towards a higher contribution from delayed cross-talk. While at lower over-voltages ($\sim 2V$) contributions are mostly equal, at high over-voltages ($\sim 8V$) the contribution of delayed cross-talk is expected

1101 to be above 80%, probably due to higher penetration depth and avalanche probability.
 1102 Results of the LCT5 7mm device from both groups mostly overlap, the slight shift between them
 1103 is most likely caused by a small error in the breakdown-voltage calculation, due to no cooling
 1104 of the tile in experiments involving light. In addition, the slope of both results seems to be mostly
 1105 equal, and the extended range measurement, overlapping with the low-range results confirms
 1106 that.
 1107 Even though results from 3 different groups mostly correlate, or are at least partially un-
 1108 derstood differences, the Optical Cross Talk of LVR 6mm Figure 47 (blue) compared to the
 1109 results from the University of Nagoya do not show any correlation at all. This is concerning,
 1110 because comparing S13360 (purple) to the same group showed strong correlation over a wide
 1111 over-voltage range. Since there is also no datasheet present yet, this device is a prototype, I
 1112 can only assume, that the device I examined is physically different than the device present at
 1113 Nagoya. It may just be a difference in coating, which combined with the TSV technology could
 1114 lead to the present uncorrelation. (quote confidential HPK talk)

1115 Missing SensL

1116 1117 7.3 Photon Detection Efficiency

1118 Since the measurement technique in this paper utilizes only dark counts and aims at giving an
 1119 understanding of the Optical Cross Talk and temperature dependencies of the different SiPMs
 1120 proposed, no PDE measurements are possible. The point of operation with the highest PDE is
 1121 determined by a different group in Japan, at the University of Nagoya. Figure (48) shows the
 1122 current results of their endeavors. The usual procedure of comparing SiPMs is done on a plot
 1123 of PDE vs OCT. This gives the most insight of the capabilities of the different devices compared
 1124 to the two proposed operating points chapter(7). Taking the PDE ascertained by the group at
 1125 Nagoya and comparing it to the resulting Optical Cross Talk from this paper produces
 1126 Figure(not yet done).

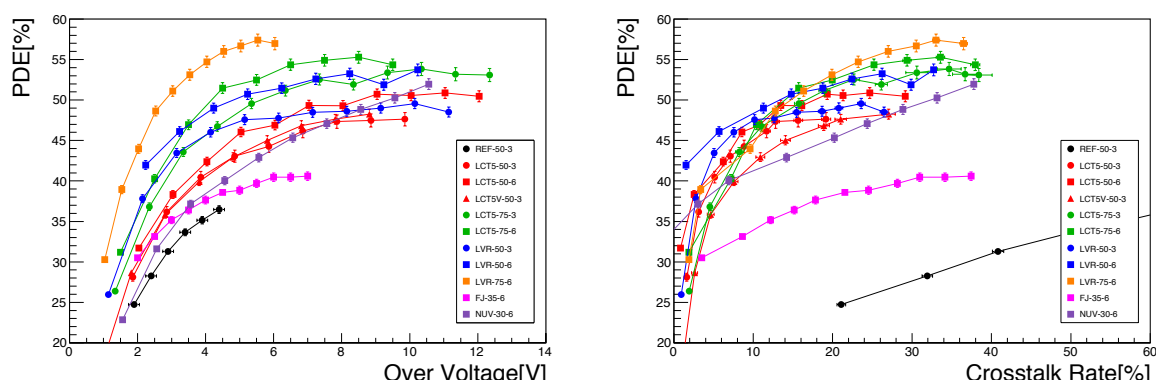


Figure 48: Photon Detection Efficiency Comparison Plots from the University of Nagoya

1127 Plotting PDE versus OCT is the standard way to compare the viability of different SiPMs, it
 1128 gives a correlated overview of the two most significant characteristics. Comparing all devices at
 1129 the two proposed points of operation produces the table in Figure(49). This table together with
 1130 Figure (not yet done) of the 5 measured devices in this thesis is used to confirm results between
 1131 groups and assist in the decision on the most viable SiPM for CHEC-S. The final decision will
 1132 be taken by the group at the University of Nagoya, by Hiro Tajima, the Photosensor work group
 1133 lead scientist? of GCT based on measurements on substantially more devices ref prelim. nagoya
 1134 table .

1135 7.4 Point of Operation Comparison 1136

Device	Min. OCT			Max. PDE		
	OCT	DCR	PDE	OCT	DCR	PDE
CHECS	15%	0.5 MHz	25% (DS)	50%	5 MHz	48% (DS)
LCT5 6mm	15%	3.4 MHz	49% (Nagoya)	22%	5 MHz	51% (Nagoya)
LCT5 7mm	15%	2.0 MHz	42% (Catania)	25%	2.5 MHz	53% (Catania)
LVR 6mm	15%	2.5 MHz	43% (Nagoya)	>27%	>6MHz	>50% (Nagoya)
SensL	15%	3.0 MHz	37% (Nagoya)	30%	6 MHz	40% (Nagoya)

Figure 49: Comparison table of the measured devices in the style of the 2 proposed operation points for CHEC-S. First point represents minimal achievable OCT, second point represents maximum achievable PDE. PDE values taken from results of other groups. Note that the LCT5 6mm device can achieve even lower OCT value ($\sim 3\%$ at $V_{ov} = 2.5$)

1137
1138

8 further analysis

8.1 multi incident probability and optical Cross Talk

1141 With increasing Dark Count Rate the probability of two dark events happening at the same
1142 time rises with increasing bias-voltage. Taking for example the Dark Count Rate of S13360 and
1143 taking the FWHM of the characteristic pulse we can calculate the probability for every dark rate
1144 at every bias-voltage and can extract a probability curve. Wouldnt that just make the DCR rise
1145 even higher since 1 2p.e. are now 2 1p.e.s' ?? nonononono

1146 multi incident has influence on optical cross talk, 2 ones are interpreted as 1 2 and are there-
1147 fore put into the 2p.e. peak of the histogram, leading to calculation errors.

8.2 Prompt and delayed cross talk ratio

1150 What happens if we take the OCT of S13360 and scale it with an expected prompt to delayed
1151 crosstalk ratio. evidence only from confidential HPK talk, need citations. Could just make new
1152 plots in HD, evaluate.

9 Conclusion and Outlook

1153 Hmhmhm
1154

1155 For that purpose 5 different SiPM from two manufacturers have been examined.

10 Glossary

- 1159 1. SiPM - Silicon Photomultiplier
- 1160 2. IACT
- 1161 3. CTA - Cherenkov Telescope Array
- 1162 4. LST
- 1163 5. MST
- 1164 6. SST
- 1165 7. GCT
- 1166 8. CHEC
- 1167 9. HPK - Hamamatsu Photonics K.K.
- 1168 10. SensL - Sense Light

119 **Bibliography**

1171 **References**

- 1173 [1] Jim Hinton et al. *Teraelectronvolt Astronomy* Ann. Rev. Astron. Astrophys., 47:523
- 1174 [2] Julien Rousselle et al. *Construction of a Schwarzschild-Couder telescope as a candidate for*
1175 *the Cherenkov Telescope Array: status of the optical system* arXiv:1509.01143v1 astro-ph.IM
- 1176 [3] The CTA Consortium *Design Concepts for the Cherenkov Telescope Array CTA, An Advanced*
1177 *Facility for Ground-Based High-Energy Gamma-Ray Astronomy* ; arXiv:1008.3703v3 [astro-
1178 ph.IM] 11 Apr 2012
- 1179 [4] Teresa Montaruli et al. *The small size telescope projects for the Cherenkov Telescope Array*
1180 *arXiv:1508.06472v1* [astro-ph.IM]
- 1181 [5] *The ASTRONET Infrastructure Roadmap* ISBN: 978-3-923524-63-1
- 1182 [6] Jim Hinton et. al *Seeing the High-Energy Universe with the Cherenkov Telescope Array As-*
1183 *troparticle Physics* 43 (2013) 1-356
- 1184 [7] R. López-Coto for the HAWC collaboration *Very high energy gamma-ray astronomy with*
1185 *HAWC* arXiv:1612.09078v1 [astro-ph.IM] 29 Dec 2016
- 1186 [8] John Murphy *SensL J-Series Silicon Photomultipliers for High-Performance Timing in Nuclear*
1187 *Medicine*
- 1188 [9] A. N. Otte et al. *Characterization of three high efficient and blue sensitive Silicon photomul-*
1189 *tipliers* arXiv:1606.05186v2 [physics.ins-det] 26 Jan 2017
- 1190 [10] A. Bouvier et al. *Photosensor Characterization for the Cherenkov Telescope Array: Silicon*
1191 *Photomultiplier versus Multi-Anode Photomultiplier Tube* ; arXiv:1308.1390v1 [astro-ph.IM]
1192 6 Aug 2013
- 1193 [11] J. Rosado S. Hidalgo *Characterization and modeling of crosstalk and afterpulsing in Hamam-*
1194 *matsu silicon photomultipliers.* arXiv:1509.02286v2 [physics.ins-det] 21 Oct 2015
- 1195 [12] Robert G. Wagner et al. *The Next Generation of Photo-Detectors for Particle Astrophysics*
1196 *arXiv:0904.3565v1* [astro-ph.IM] 22 Apr 2009
- 1197 [13] *Opto-semiconductor handbook Chapter 03 Si APD, MPPC.* Hamamatsu Photonics K.K.
- 1198 [14] Maurice Stephan. *Design and Test of a Low Noise Amplifier for the Auger Radio Detector*
1199 *Diploma Thesis, RWTH Aachen University, Juli 2009*

-
- 1200 [15] Benjamin Glauß. *Optical Test Stand and SiPM characteriation studies*. Master's Thesis,
1201 RWTH Aachen University, June 2012.
- 1202 [16] http://astro.desy.de/gamma_astronomy/cta/index_eng.html
- 1203 [17] <http://www.ung.si/en/research/laboratory-for-astroparticle-physics/>
1204 projects/cta/
- 1205 [18] <http://www.ung.si/en/research/laboratory-for-astroparticle-physics/>
1206 projects/fermi-lat/
- 1207 [19] http://212.71.251.65/aspera//index.php?option=com_content&task=blogcategory&id=111&Itemid=234
1208

12 Appendix

A CTA

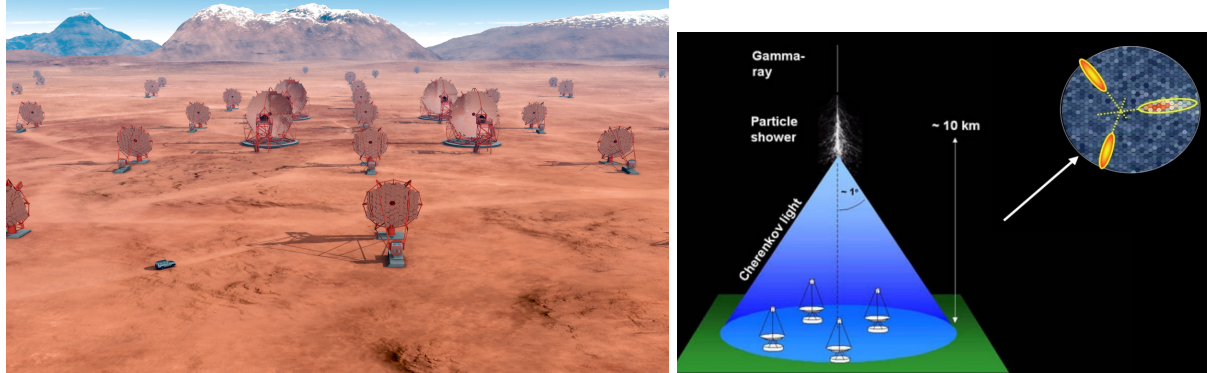


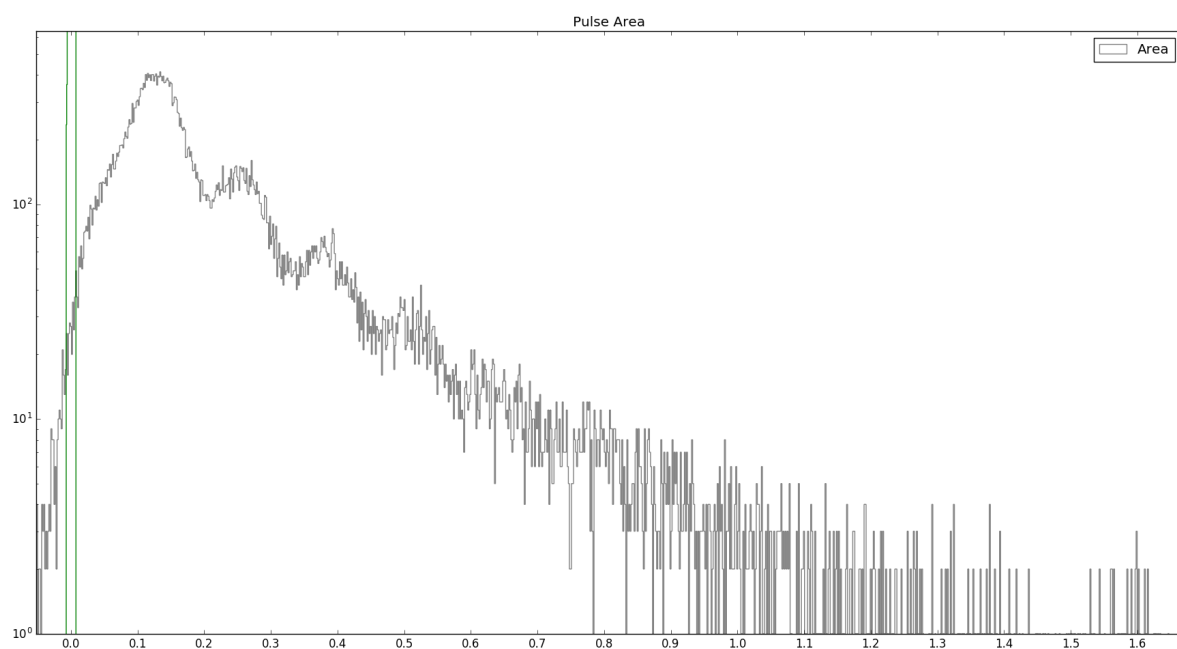
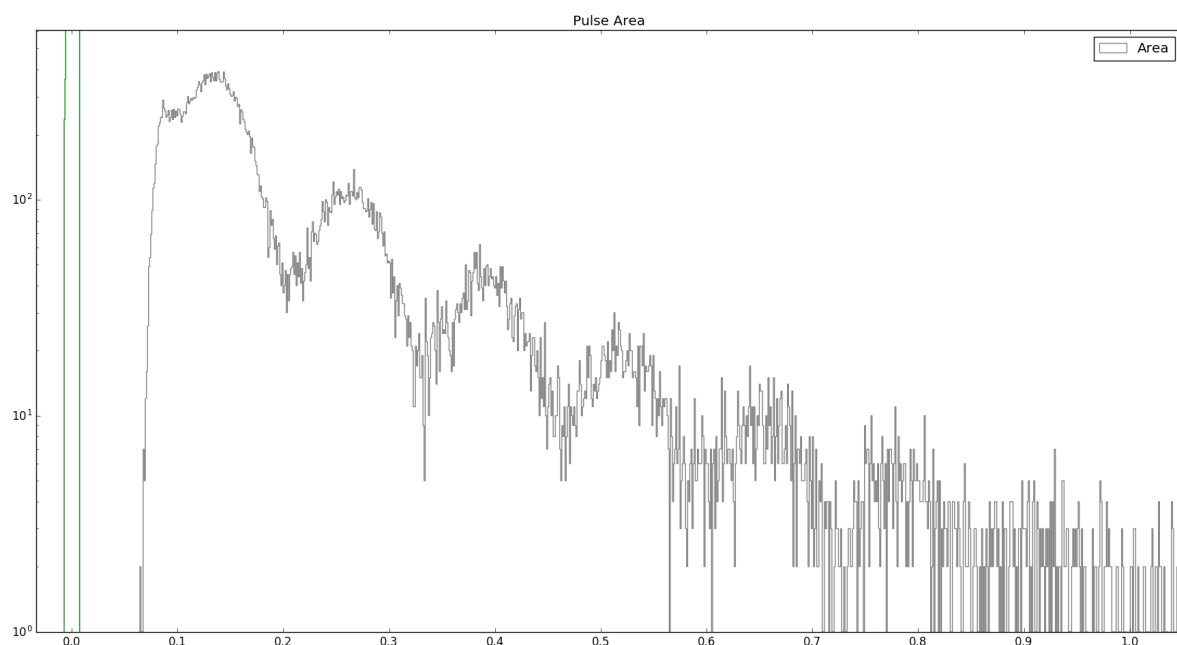
Figure 50: A render of the finished CTA Array at the site in Namibia (left) with visible LSTs and MSTs, and the Shower Path Reconstruction technique of the stereoscopic view employed by current IACT experiments like HESS, MAGIC, VERITAS (right).

B progenitor experiments of CTA



Figure 51: IACT Projects: HESS in the Khomas Highland, Namibia. MAGIC at the Roque de los Muchachos Observatory on La Palma , one of the Canary Islands. VERITAS at Mount Hopkins, Arizona, USA

C Pulse Area Spectra of different integration window widths



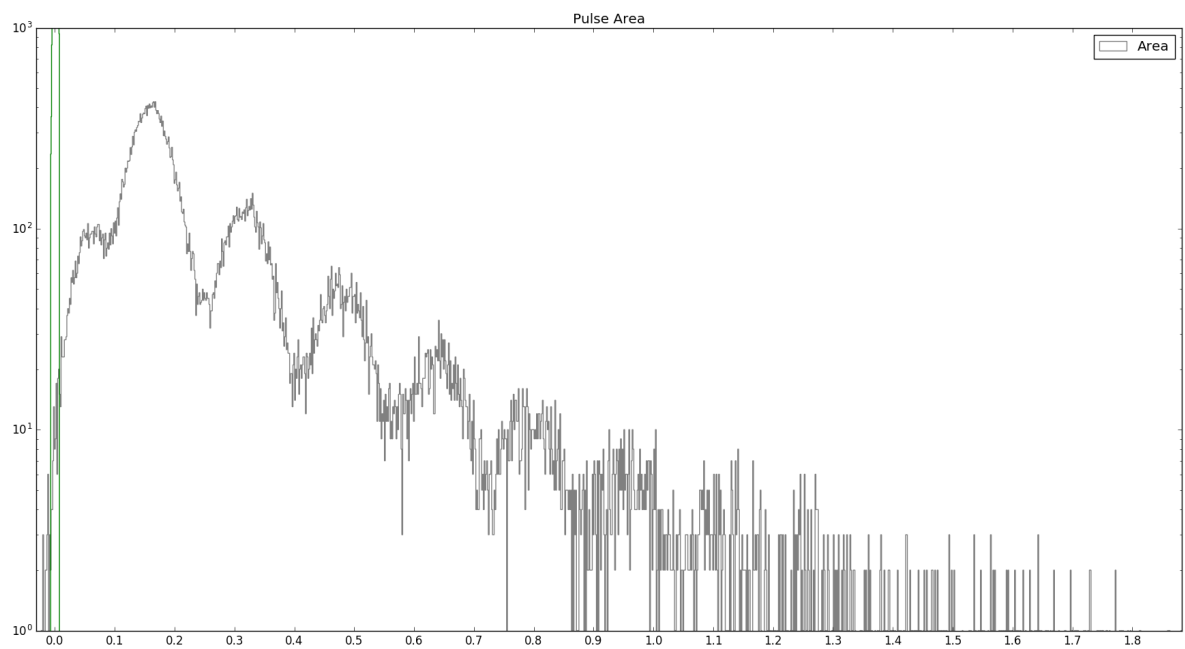


Figure 52: Pulse Area Spectra with window widths of 5 left 5 right (top), 5 left 20 right (middle), 10 left 10 right (bottom) bins respectively. Left of the 1p.e. peak of the top picture a part of the 0p.e. peak is visible. The middle figure shows the distortion an asymmetrical integration window causes. The bottom figure is the employed integration window to derive the pulse area histogram.

D BreakdownVoltage

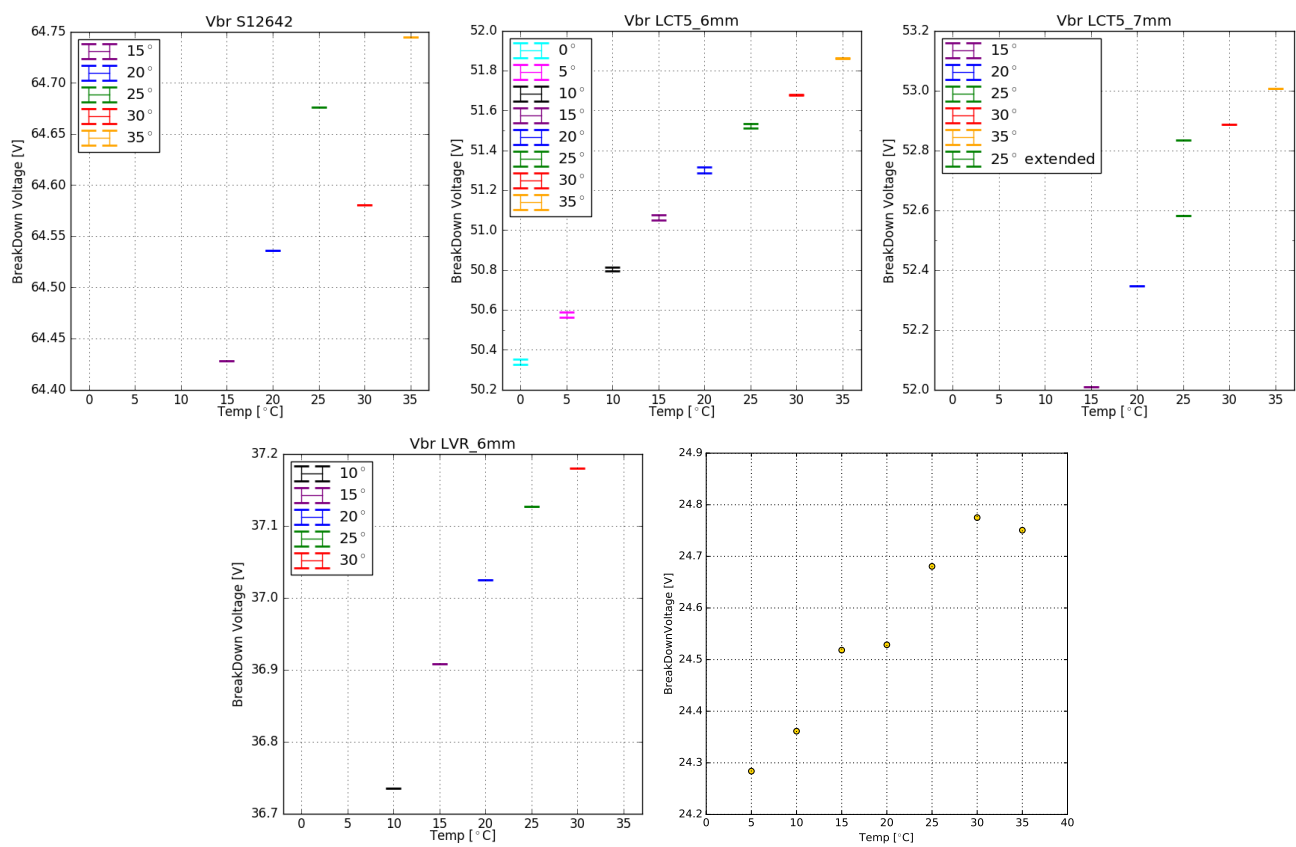


Figure 53: Dependency of the breakdown-voltage of temperature for the 5 measured devices.

For LCT5 7mm , the extended range measurement adds an extra datapoint at 25°C
 HPK S12642 (CHEC-S) (top left) ; HPK LCT5 6mm (top middle) ; HPK LCT5 7mm (top right) ; HPK LCT5 LVR 6mm (bottom left) ; SensL FJ60035 (bottom right).

Device	$\Delta V / T$ [mV/°C]
CHECS	13.1 ± 4.1
LCT5 6mm	43.5 ± 0.4
LCT5 7mm	53.0 ± 4.0
LVR 6mm	25.6 ± 2.6
SensL	15.0 ± 1.1

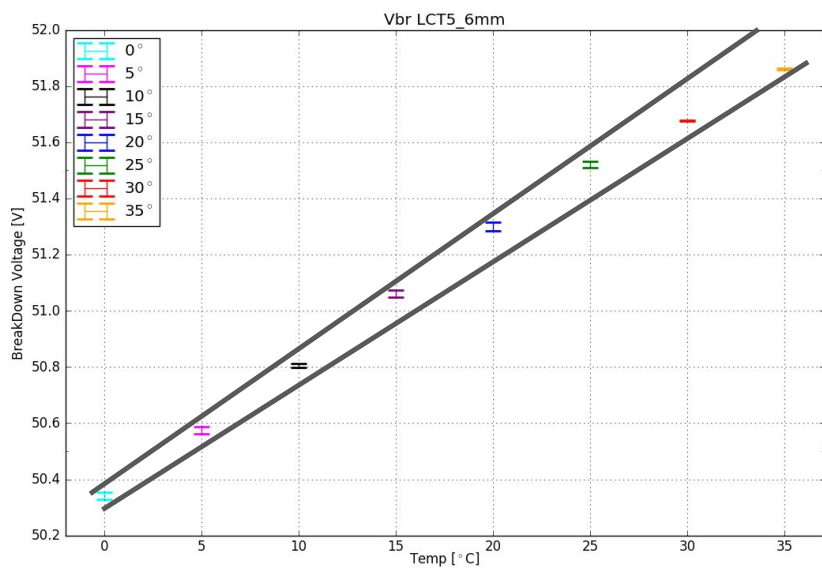


Figure 54: The extracted breakdown-voltage dependence of all measured devices, derived from two regression lines and their mean. For some devices the breakdown-voltage dependency is known through datasheet values. S12642 = 60mV/°C, S13360 = 54mV/°C, SensL FJ60035 =<21.5mV/°C

1219
1220

E Pulse Area and Height Spectra

1221 Example pulse area spectra

F CHEC-S pixel comparison

1224 Comparison of results from 10 different pixels on the CHEC-S (HPK S12642-1616PA-50) array.
 1225 Every pixel is analyzed with the same technique and analysis parameters.

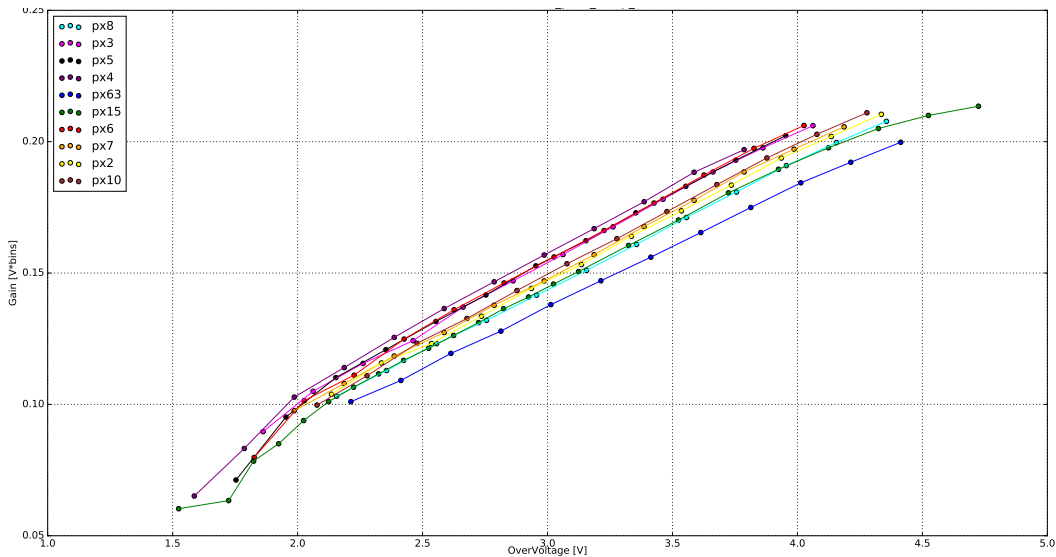


Figure 55: Gain comparison of 10 different pixels of the CHEC-S (HPK S12642-1616PA-50) array

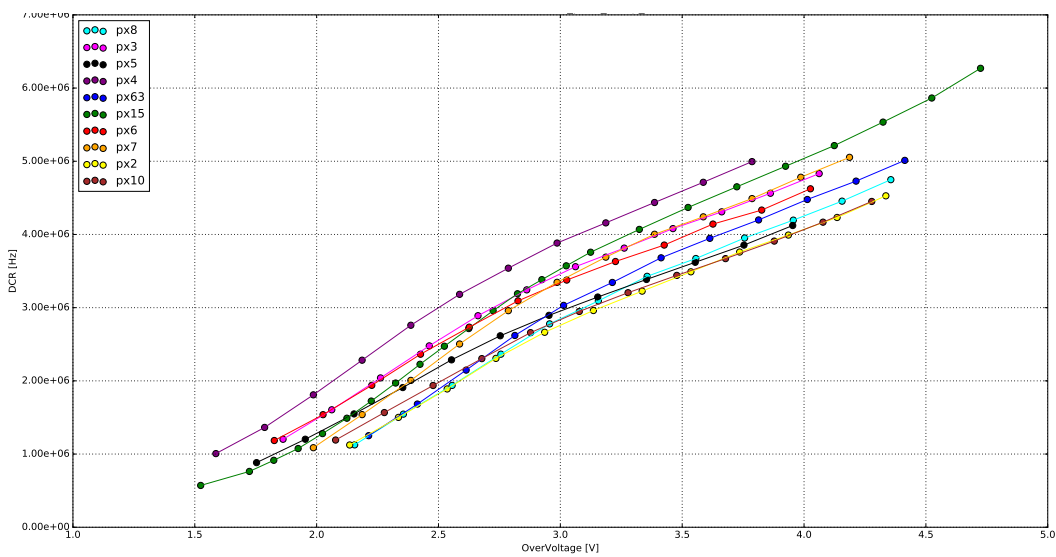


Figure 56: DCR comparison of 10 different pixels of the CHEC-S (HPK S12642-1616PA-50) array

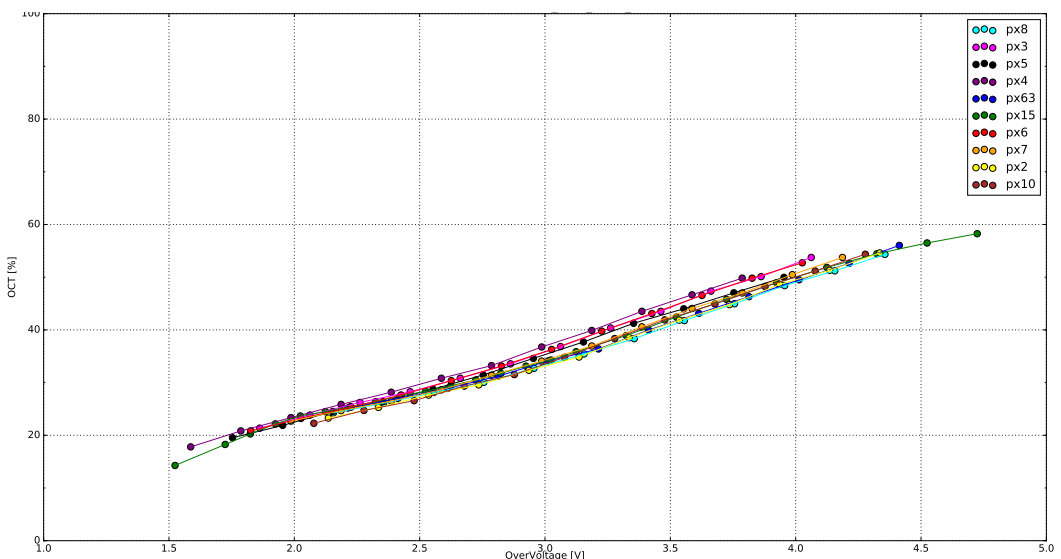


Figure 57: OCT comparison of 10 different pixels of the CHEC-S (HPK S12642-1616PA-50) array

G Additional Data Analysis Plots

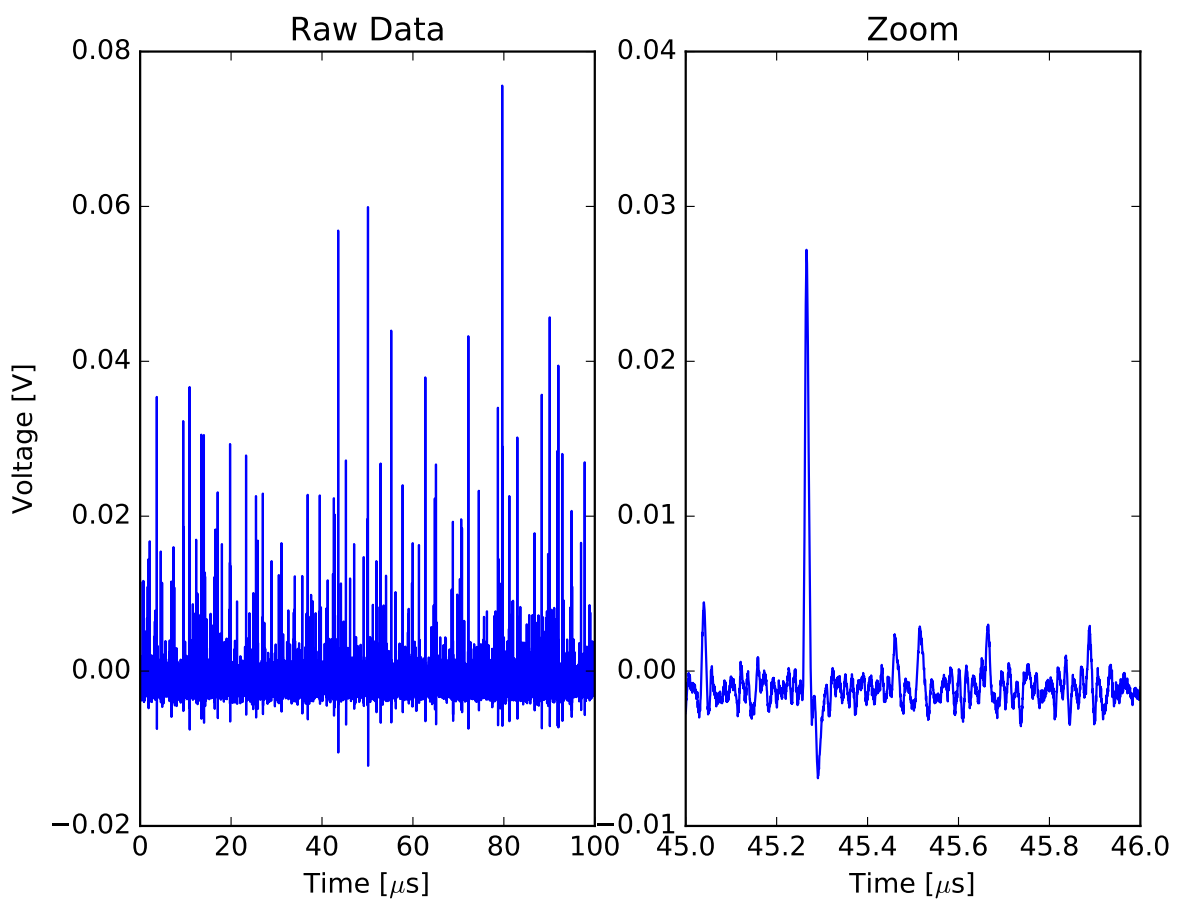


Figure 58: Description

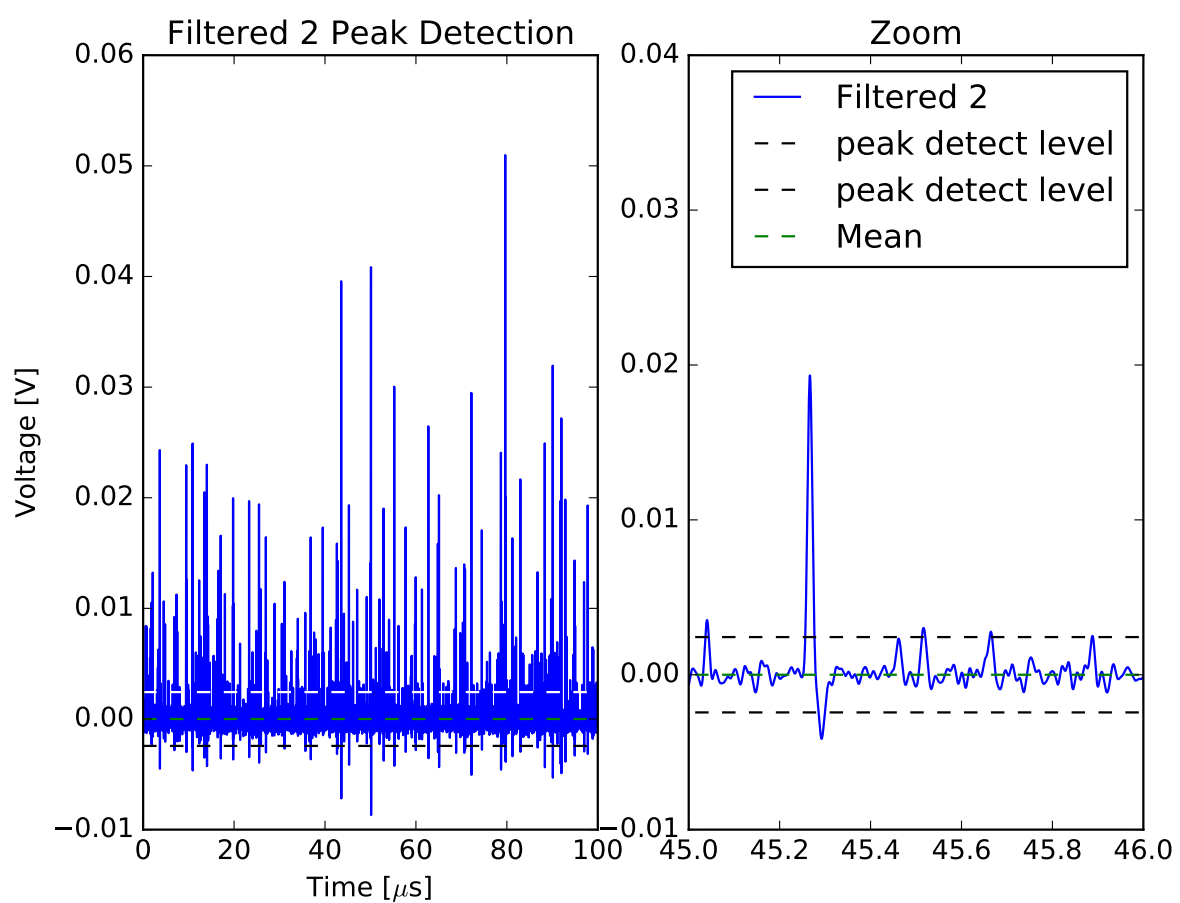


Figure 59: Description

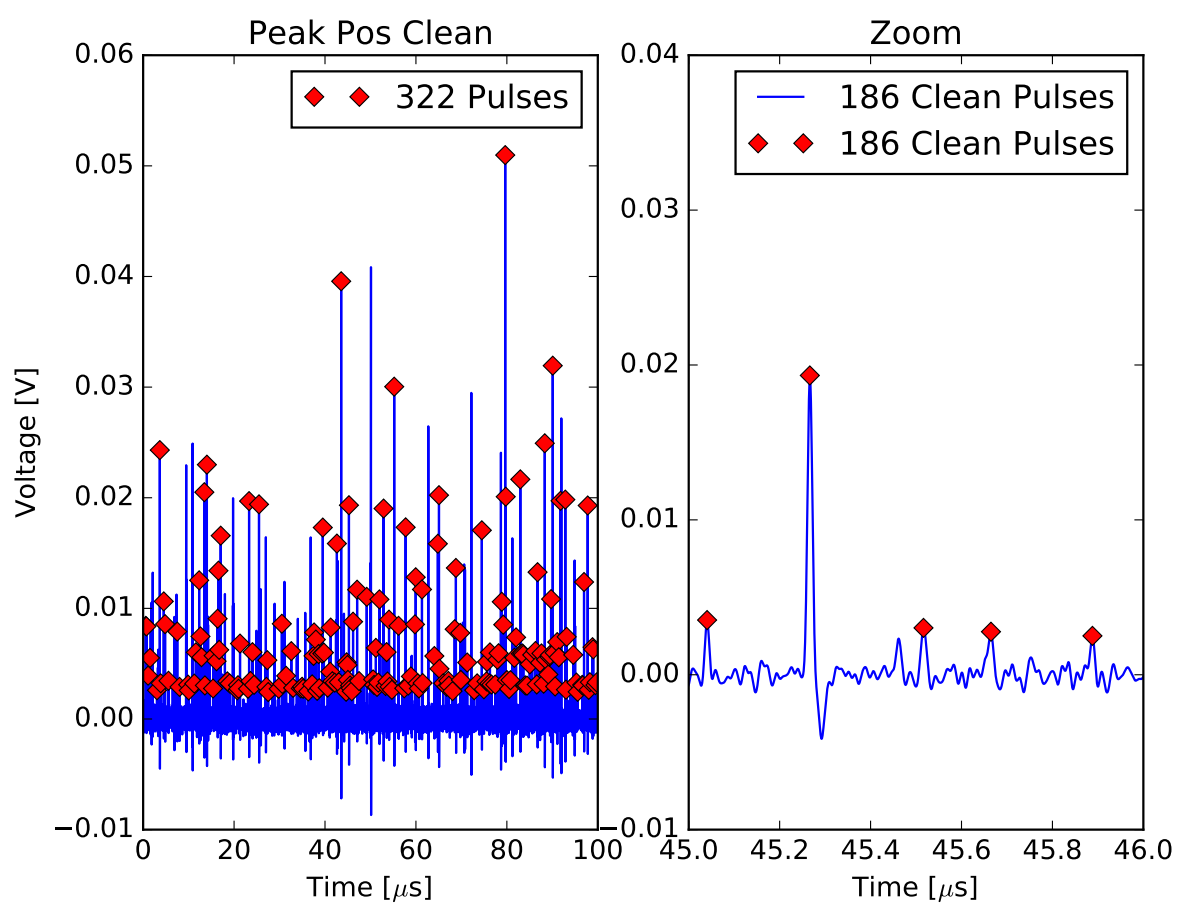


Figure 60: Description

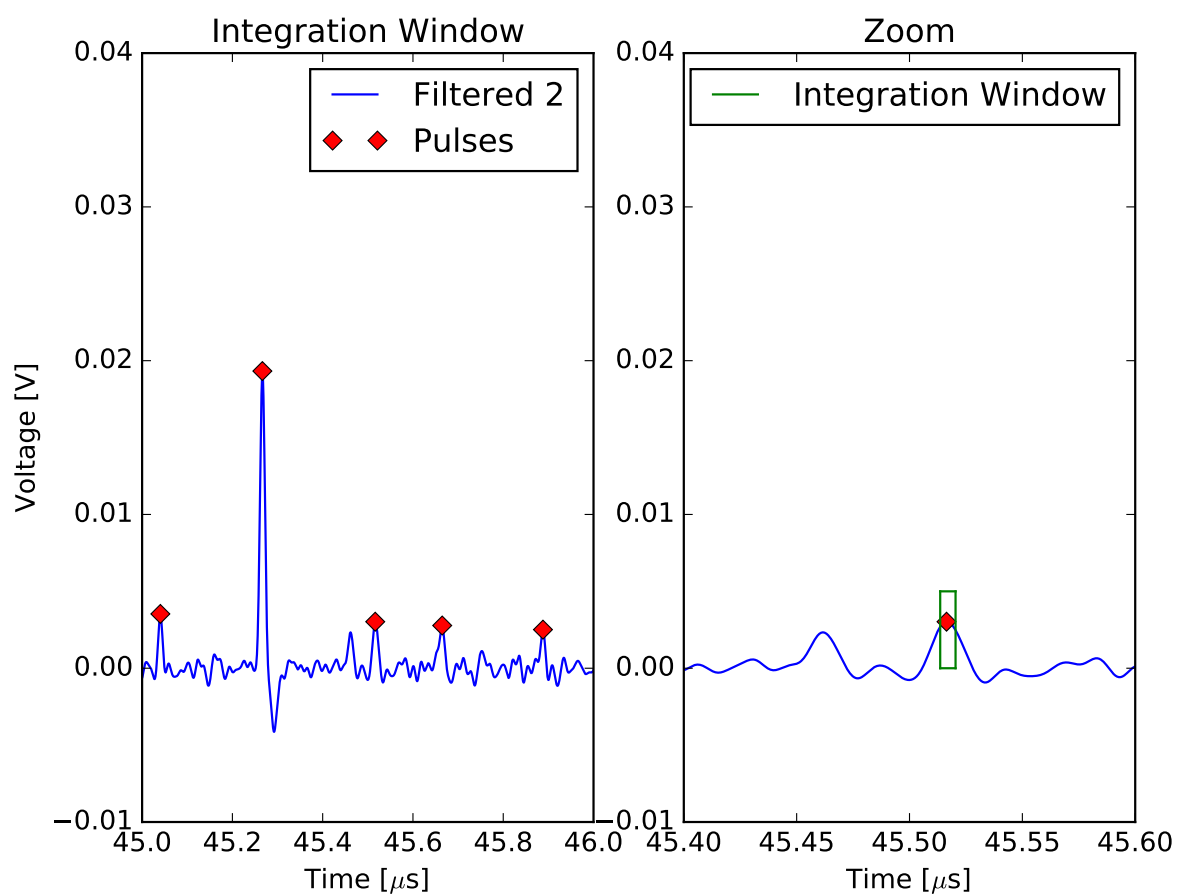


Figure 61: Description

¹²²⁸ Erklärung zur Master-Thesis

¹²²⁹ Hiermit versichere ich, die vorliegende Master-Thesis ohne Hilfe Dritter nur mit
¹²³⁰ den angegebenen Quellen und Hilfsmitteln angefertigt zu haben. Alle Stellen, die
¹²³¹ aus Quellen entnommen wurden, sind als solche kenntlich gemacht. Diese Arbeit
¹²³² hat in gleicher oder ähnlicher Form noch keiner Prüfungsbehörde vorgelegen.

¹²³³ Darmstadt, den April 19, 2017

¹²³⁴ _____

¹²³⁵ (B. Gebhardt)
